Universität Bremen

Master Thesis

Assembly and Test of a DOAS Measurement System for Outdoor Applications

Program:

M.Sc. Space Sciences and Technologies

Submitted by:

Marian Paul, 6176365

Submitted to:

Dr. Andreas Richter

Prof. Dr. Annette Ladstätter-Weißenmayer

Institute of Environmental Physics

University of Bremen

Bremen, Germany

September 11, 2025

Universität Bremen

Eigenständigkeits- und Einverständniserklärung zur Überprüfung mit Plagiatssoftware sowie die Erklärung zur Veröffentlichung bei Bachelor- und Masterarbeiten

Declarations of Authorship and Consent for Checking with Plagiarism Software and the Declaration of Publication for Bachelor's and Master's Thesis

Studierenden-Angaben / Student Information:

Matrikelnr./ Student ID	**6176365**
Nachname / Surname	**Paul**
Vorname / First Name	**Marian**

Titel der Arbeit / Title of Thesis

Assembly and Test of a DOAS Measurement System for Outdoor Applications

A) Eigenständigkeitserklärung / Declaration of Authorship

Ich versichere, dass ich die vorliegende Arbeit selbstständig verfasst und keine anderen als die angegebenen Quellen und Hilfsmittel verwendet habe. Alle Teile meiner Arbeit, die wortwörtlich oder dem Sinn nach anderen Werken entnommen sind, wurden unter Angabe der Quelle kenntlich gemacht. Gleiches gilt auch für Zeichnungen, Skizzen, bildliche Darstellungen sowie für Quellen aus dem Internet, dazu zählen auch KI-basierte Anwendungen oder Werkzeuge.
Die Arbeit wurde in gleicher oder ähnlicher Form noch nicht als Prüfungsleistung eingereicht.

I hereby affirm that I have written the present work independently and have used no sources or aids other than those indicated. All parts of my work that have been taken from other works, either verbatim or in terms of meaning, have been marked as such, indicating the source. The same applies to drawings, sketches, pictorial representations and sources from the Internet, including AI-based applications or tools. The work has not yet been submitted in the same or a similar form as a final examination paper.

☑ Ich habe KI-basierte Anwendungen und/oder Werkzeuge genutzt und diese im Anhang "Nutzung KI basierte Anwendungen" dokumentiert.

I have used AI-based applications and/or tools and documented them in the appendix "Use of AI-based applications".

B) Erklärung zur Veröffentlichung von Bachelor- oder Masterarbeiten
Declaration regarding the publication of bachelor's or master's thesis

Die Abschlussarbeit wird zwei Jahre nach Studienabschluss dem Archiv der Universität Bremen zur dauerhaften Archivierung angeboten. Archiviert werden:

Two years after graduation, the thesis is offered to the archive of the University of Bremen for permanent archiving. The following are archived:

1) Masterarbeiten mit lokalem oder regionalem Bezug sowie pro Studienfach und Studienjahr 10 % aller Masterarbeiten
Master's theses with a local or regional focus, as well as per subject and academic year 10% of all Master's thesis

2) Bachelorarbeiten des jeweils ersten und letzten Bachelorabschlusses pro Studienfach und Jahr.
Bachelor's thesis for the first and last bachelor's degrees per subject and year.

☑ Ich bin damit einverstanden, dass meine Abschlussarbeit im Universitätsarchiv für wissenschaftliche Zwecke von Dritten eingesehen werden darf.
I agree that my thesis may be viewed by third parties in the university archive for academic purposes.

☑ Ich bin damit einverstanden, dass meine Abschlussarbeit nach 30 Jahren (gem. §7 Abs. 2 BremArchivG) im Universitätsarchiv für wissenschaftliche Zwecke von Dritten eingesehen werden darf.
I agree that my thesis may be viewed by third parties for academic purposes in the university archive after 30 years (in accordance with §7 para. 2 BremArchivG).

☐ Ich bin **nicht** damit einverstanden, dass meine Abschlussarbeit im Universitätsarchiv für wissenschaftliche Zwecke von Dritten eingesehen werden darf.
I do not consent to my thesis being made available in the university archive for third parties to view for academic purposes.

C) Einverständniserklärung zur elektronischen Überprüfung der Arbeit auf Plagiate
Declaration of consent for electronic checking of the work for plagiarism

Eingereichte Arbeiten können nach § 18 des Allgemeinen Teil der Bachelor- bzw. der Masterprüfungsordnungen der Universität Bremen mit qualifizierter Software auf Plagiatsvorwürfe untersucht werden.
Zum Zweck der Überprüfung auf Plagiate erfolgt das Hochladen auf den Server der von der Universität Bremen aktuell genutzten Plagiatssoftware.

Submitted papers can be checked for plagiarism using qualified software in accordance with § 18 of the General Section of the Bachelor's or Master's Degree Examination Regulations of the University of Bremen. For the purpose of checking for plagiarism, the upload to the server is done using the plagiarism software currently used by the University of Bremen.

☑ Ich bin damit einverstanden, dass die von mir vorgelegte und verfasste Arbeit zum oben genannten Zweck dauerhaft auf dem externen Server der aktuell von der Universität Bremen genutzten Plagiatssoftware, in einer institutionseigenen Bibliothek (Zugriff nur durch die Universität Bremen), gespeichert wird.

I agree that the work I have submitted and written will be stored permanently on the external server of the plagiarism software currently used by the University of Bremen, in a library belonging to the institution (accessed only by the University of Bremen), for the above-mentioned purpose.

☐ Ich bin **nicht** damit einverstanden, dass die von mir vorgelegte und verfasste Arbeit zum o.g. Zweck dauerhaft auf dem externen Server der aktuell von der Universität Bremen genutzten Plagiatssoftware, in einer institutionseigenen Bibliothek (Zugriff nur durch die Universität Bremen), gespeichert wird.

I do not consent to the work I submitted and wrote being permanently stored on the external server of the plagiarism software currently used by the University of Bremen, in a library belonging to the institution (accessed only by the University of Bremen), for the above-mentioned purpose.

Das Einverständnis der dauerhaften Speicherung des Textes ist freiwillig. Die Einwilligung kann jederzeit durch Erklärung gegenüber der Universität Bremen, mit Wirkung für die Zukunft, widerrufen werden. Weitere Informationen zur Überprüfung von schriftlichen Arbeiten durch die Plagiatsoftware sind im Nutzungs- und Datenschutzkonzept enthalten. Diese finden Sie auf der Internetseite der Universität Bremen.

Consent to the permanent storage of the text is voluntary. Consent can be withdrawn at any time by making a declaration to this effect to the University of Bremen, with effect for the future. Further information on the checking of written work using plagiarism software can be found in the data protection and usage concept. This can be found on the University of Bremen website.

Mit meiner Unterschrift versichere ich, dass ich die obenstehenden Erklärungen gelesen und verstanden habe und bestätige die Richtigkeit der gemachten Angaben.

With my signature, I confirm that I have read and understood the above explanations and confirm the accuracy of the information provided.

16.09.2025 M. [signature]

Datum / Date Unterschrit/ Signature

Abstract

Air pollution poses a threat to human health and is closely linked to climate change as air polluting species are emitted in the same combustion processes as greenhouse gases. Therefore, accurate measurement and monitoring of air pollutants such as NO_2 is crucial. Differential Optical Absorption Spectroscopy (DOAS) is a well-established method of quantifying the atmospheric abundance of trace gases, but it is prone to unwanted spectral shift due to variations in ambient temperature. Existing measurement systems are usually large, expensive, or not thermally stabilized.

In this thesis a portable DOAS measurement system is developed using a thermally insulated Zarges box controlled with a thermoelectric module. The temperature control is implemented with a PID controller.

To verify functionality, the Zarges DOAS measurement system undergoes thermal testing in a laboratory with small temperature fluctuations, on a rooftop with larger variations, and in a core repository with relatively low temperatures. These tests show that the system exhibits good thermal stability, but required controller re-tuning, as it was prone to temperature oscillations under certain conditions.

The measurement system is compared to the established IUPB MAX-DOAS instrument to validate accuracy and reliability. The comparison shows that the Zarges DOAS measurement system delivers high-quality data and, due to its high temperature stability, produces a very small spectral shift that is one order of magnitude smaller than that of the IUPB MAX-DOAS.

During the outdoor tests, humidity seeped into the Zarges DOAS measurement system, suggesting that further adaptations are necessary before a long-term outdoor deployment.

Contents

List of Figures

1. Introduction

Air pollution is an ongoing problem and a threat to human health, imposing risk of cardiovascular and respiratory diseases, as well as cancer. Data of the World Health Organization (WHO) have shown that 99 % of the world population are exposed to polluted air, exceeding the WHO guideline limits. Inhabitants of low- and middle-income countries are particularly vulnerable to this exposure [1]. Air pollution is also closely linked to climate change, as major air pollutants are released in the same fossil fuel combustion processes, in transport, and from industrial facilities as greenhouse gases. Monitoring air pollutants is therefore crucial.

Differential optical absorption spectroscopy (DOAS) is a well-established method of quantifying atmospheric abundance of polluting trace gases such as NO_2 [2]. However, DOAS instruments are prone to deterioration of data quality due to temperature fluctuations. Existing measurement systems, capable of providing accurate measurement data, are usually large, expensive or not thermally stabilized. Therefore, this thesis aims to establish a portable, easy-to-setup and thermally stabilized DOAS measurement system, which is suitable for outdoor applications. It presents the design, assembly, and testing of such a system.

The goal is achieved by establishing a theoretical foundation, including an overview over the atmospheric composition, radiative transfer, and absorption spectroscopy with a focus on the background of the DOAS technique, as well as the basics of thermal control. Essential parts of the design are the choice of thermoelectric components as a result of the estimated heat load, and the planning of the physical layout of the components, which is described in Chapter 3. The completed measurement system undergoes extended testing to assess the performance of the thermal control and comparison against the established IUPB MAX-DOAS instrument to validate accuracy and reliability of the measurement system. These tests and comparisons are shown in Chapter 4. The thesis closes with a short discussion of limitations and potential improvements for future deployments.

2. Theoretical Background

2.1 Atmospheric Composition and Vertical Structure

The atmosphere is a layer of gases that surrounds the Earth. It mainly consists of the bulk gases molecular nitrogen (N_2), molecular oxygen (O_2) and the noble gas argon (Ar) that make up 99.9 % of the dry atmosphere [2]. The remaining 0.1 % are shared by a large number of trace gases. The typical atmospheric constituents and their concentrations can be found in Table 2.1.

Table 2.1: Typical constituents of the atmosphere[3]

Constituent	**Molecular Weight**	**Fractional Concentration**
Nitrogen (N_2)	28.013	78.08%
Oxygen (O_2)	32.000	20.95%
Argon (Ar)	39.95	0.93%
Water vapor (H_2O)	18.02	0–5%
Carbon dioxide (CO_2)	44.01	407 ppm [4]
Neon (Ne)	20.18	18 ppm
Helium (He)	4.00	5 ppm
Methane (CH_4)	16.04	1.75 ppm
Krypton (Kr)	83.80	1 ppm
Hydrogen (H_2)	2.02	0.5 ppm
Nitrous oxide (N_2O)	56.03	0.3 ppm
Ozone (O_3)	48.00	0–0.1 ppm

Water vapor has a rather short lifetime in the atmosphere and its atmospheric concentration is highly variable over time and location. It ranges from 10 ppmv in the coldest regions of the atmosphere to 5 % in the hot and humid regions [3]. Except for water vapor and the greenhouse gases CO_2, CH_4, and N_2O, which increase due to anthropogenic emissions, as well as O_3, whose concentration varies strongly with factors such as diurnal cycles, seasonal variations, and pollution levels, the concentrations of the gases listed in Table 2.1 are relatively stable over time. These stable gases are therefore called permanent atmospheric constituents [2].

The vertical structure of the atmosphere can be determined by its temperature gradient, its mixing mechanisms, or its degree of ionization (see Figure 2.1). In terms of temperature, Earth's atmosphere is divided into troposphere, stratosphere, mesosphere, and thermosphere. The troposphere is the

atmospheric layer where humans live and, hence, where most air pollutants are emitted. It consists of the atmospheric boundary layer, where friction with the Earth's surface influences the movement and mixing of air [2], and the free troposphere. The temperature decreases with height in the troposphere. The stratosphere is a poorly mixed layer with a positive temperature gradient, caused by the absorption of solar ultraviolet radiation by ozone. Above the stratosphere, the upper atmosphere is divided into the mesosphere, the thermosphere, and the exosphere.

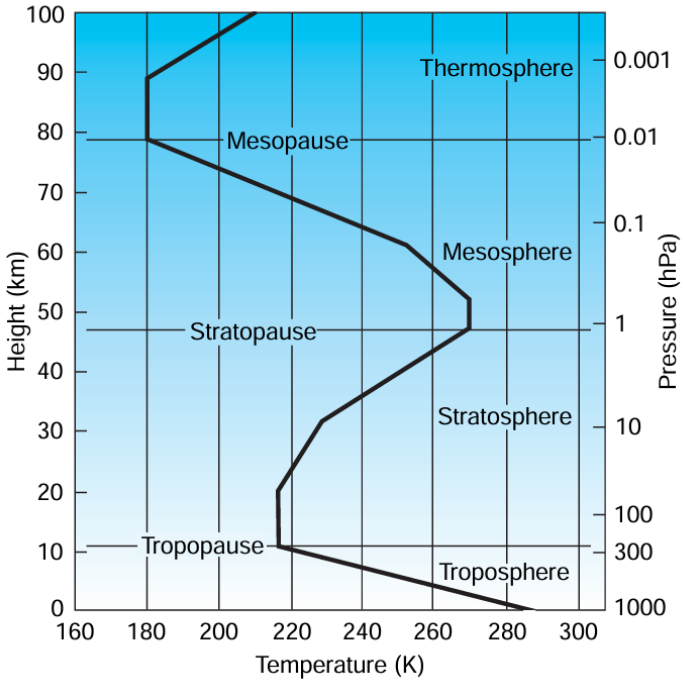

Figure 2.1: Vertical structure of the atmosphere [3]

The pressure in the atmosphere is governed by the barometric equation:

$$\mathrm{p(z) = p_o \cdot \exp\left(-\frac{Mgz}{RT}\right)} \tag{2.1}$$

Where p_o is the pressure at a reference level (commonly sea level), M is the molar mass of air, g is the gravitational acceleration, z denotes the height, R is the universal gas constant and T is the temperature. Equation 2.1 shows that with height, the pressure decreases exponentially. The density behaves in the same way [3].

Air Pollution

Nitrogen oxides $NO_x = NO + NO_2$ are among the main pollutants, causing poor air quality and eventually affecting human health [5]. There are natural and anthropogenic sources of NO_x. The

main natural sources are forest fires, lightning storms, and emissions from the soil. Anthropogenic sources are combustion processes, particularly combustion of fossil fuels in power plants, industry and heating as well as transport (e.g. cars, aircraft, ships) [2]. Nitrogen oxides are mainly released into the troposphere as nitric oxide (NO), which is quickly converted to NO_2 (see Reaction 3)[3]. In the northern hemisphere, human activities account for 90 % of the NO emissions [6].

Nitrogen oxides play an important role in atmospheric chemistry, especially in tropospheric ozone formation. When mixtures of NO_x and volatile organic compounds (VOCs) are exposed to UV radiation, ozone is produced. Photolysis of NO_2 leads to the production of $O(^3P)$, which recombines with O_2 and ultimately forms ozone (see Reactions R1 and R2) [2].

$$NO_2 \xrightarrow{h\nu} NO + O(^3P), \tag{R1}$$

$$O(^3P) + O_2 + M \longrightarrow O_3 + M, \tag{R2}$$

In Reaction R2 M is any atmospheric molecule. Photolysis of each NO_2 molecule creates one O_3 molecule, since other reactions of $O(^3P)$ are negligible under tropospheric conditions [2]. Ozone rapidly oxidizes NO to NO_2, thereby completing the photostationary cycle:

$$O_3 + NO \longrightarrow NO_2 + O_2, \tag{R3}$$

The photostationary state relation between NO, NO_2 and O_3 is called the Leighton relationship [3], which is presented as:

$$[O_3] = \frac{j[NO_2]}{k_2[NO]} \tag{2.2}$$

where j is the NO_2 photolysis frequency, k_2 is the rate constant for the reaction of O_3 with NO_2 and the square brackets denote concentrations of the respective species.

Reactions R1 to R3 create a null cycle. That means that no net ozone is produced. However, in the presence of VOCs NO can be converted to NO_2 through reaction pathways that do not involve ozone and thereby break the null cycle leading to net ozone production. While stratospheric ozone, which accounts for about 90 % of the atmosphere's ozone abundance, reduces the intensity of the UV radiation from the sun and, therefore, is beneficial for human health, tropospheric ozone is harmful to plants and humans due to its reactivity [3].

2.2 Radiative Transfer

The retrieval of NO_2 abundances with DOAS relies on the interaction of solar radiation with matter along the light path. This section introduces the basic concepts of radiative transfer. In the first approximation the sun can be imagined as a black body. A black body is a surface that absorbs all incoming radiation and only emits radiation according to Planck's law [3]:

$$\mathrm{I}(\lambda, \mathrm{T}) = \frac{2\pi \mathrm{hc}^2}{\lambda^5 (\exp\left(\frac{\mathrm{hc}}{\lambda \mathrm{k_B T}}\right) - 1)} \tag{2.3}$$

where h denotes Planck's constant, c denotes the speed of light in vacuum, λ is the wavelength, k_B is Boltzmann's constant and T is the temperature. The law links the intensity of emitted radiation at a certain wavelength to the emitter's temperature. Following that relationship, the sun's emitted spectrum looks like depicted in Figure 2.2

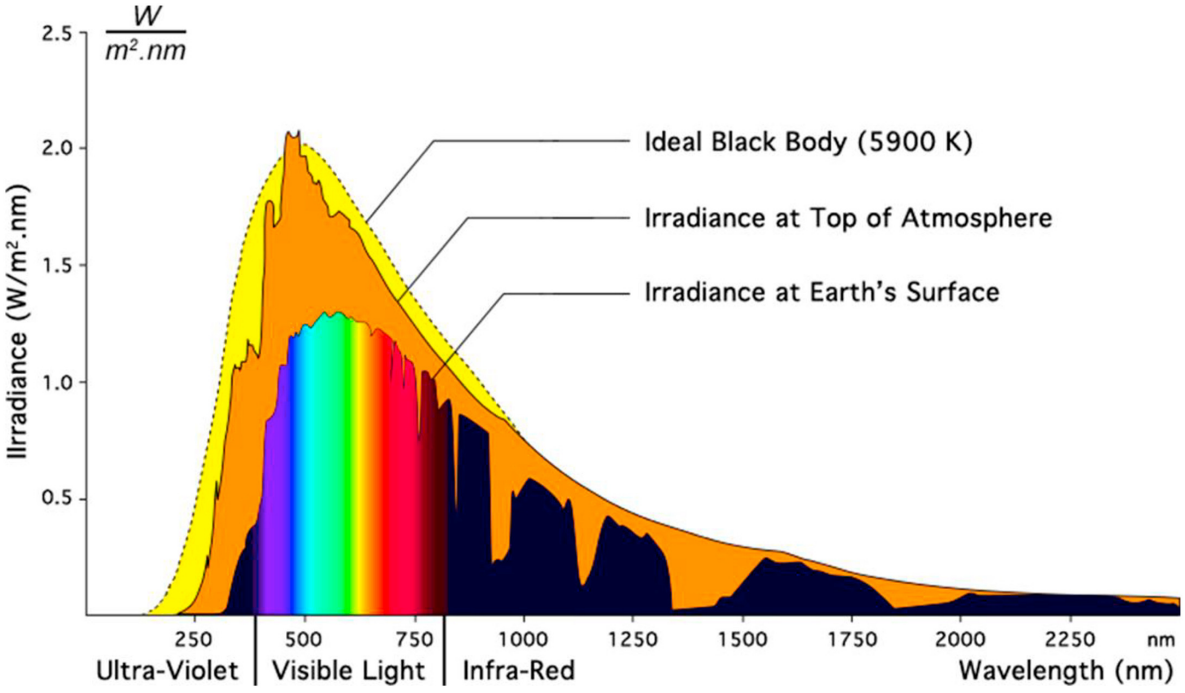

Figure 2.2: Solar irradiance depending on wavelength[7]

It can be seen that the maximum of the solar irradiance is in the visible spectral range. The solar spectrum differs slightly from the expected radiation of a blackbody at sun's temperature. Those differences are due to absorptions by various species in the sun's photosphere and chromosphere. Those absorption lines are known as Fraunhofer lines [8]. The solar irradiance is also attenuated by scattering and absorption in the atmosphere of the Earth, not only by molecules, but also by aerosols.

Scattering

There are multiple forms of scattering. Elastic scattering alters the propagation direction of a photon without changing its energy, and inelastic scattering also changes the photon's energy (Raman scattering). Rayleigh scattering is a form of elastic scattering, that occurs on small particles. More precisely, there is a size parameter given by:

$$\mathrm{x} = \frac{2\pi \mathrm{r}}{\lambda} \tag{2.4}$$

with r being the particle's radius and λ being the wavelength. When $x \ll 1$ the Rayleigh scattering regime is followed with a scattering efficiency of

$$\mathrm{K}_\lambda \propto \lambda^{-4} \tag{2.5}$$

Equation 2.5 shows that Rayleigh scattering is highly wavelength dependent. For a size parameter of $0.1 \leq x \leq 50$ the Mie scattering regime is in effect. In this regime the scattering efficiency shows the behavior of a dampened oscillation with a mean around 2. Mie scattering has a smaller wavelength dependency. In contrast to the Rayleigh regime, where radiation is scattered evenly in forward and backward direction, in the Mie regime radiation is more likely to be scattered in the forward direction [3].

Absorption

Absorption is the process in which radiation interacts with matter (e.g. atoms, molecules, etc.) in such a way that the matter gains energy, undergoing a transition from a low-energy state to a higher-energy state, while the radiation intensity is reduced [9].

In atoms and molecules energy states are discrete. Therefore, the photon's energy needs to match the energy difference between two states to be absorbed. The photon energy is defined as:

$$E = h\nu \tag{2.6}$$

where h denotes Planck's constant and $\nu = \frac{c}{\lambda}$ is the frequency of the radiation. The possible transitions and their respective energies are:

- Electronic transitions: the transition energies are in the order of 1 eV. Hence, electronic transitions correspond to the visible and UV spectral range.
- Vibrational transitions: vibrational transition energies are in the order of 0.1 eV, corresponding to the IR spectral range.

- Rotational transitions: transition energies are in the order of 1×10^{-3} eV to 1×10^{-2} eV, which corresponds to the sub-mm and microwave range.

[2]

2.3 Spectroscopy

To measure the amount of specific trace gas species, absorption spectroscopy is used. Absorption spectroscopy makes use of the interaction of matter with electromagnetic radiation and relies on the wavelength dependence of the absorption spectra. The core setup for the spectroscopic measurements used in this thesis consists of a telescope to gather the light, a Czerny-Turner spectrometer to separate the spectral components of the incoming radiation, and a charge-coupled device (CCD) detector to record the intensity of spectrally resolved light for quantitative analysis. This analysis is done with the Differential Optical Absorption Spectroscopy (DOAS) technique to quantify the slant column densities and ultimately the vertical column densities of given trace gas species. [2]

2.3.1 Functional Principle of a Czerny-Turner Spectrometer

The Czerny-Turner configuration forms the basis for a straightforward spectrometer. Its components are an entrance slit, two concave mirrors, a reflection grating, and a CCD detector. Its geometry can be seen in Figure 2.3.

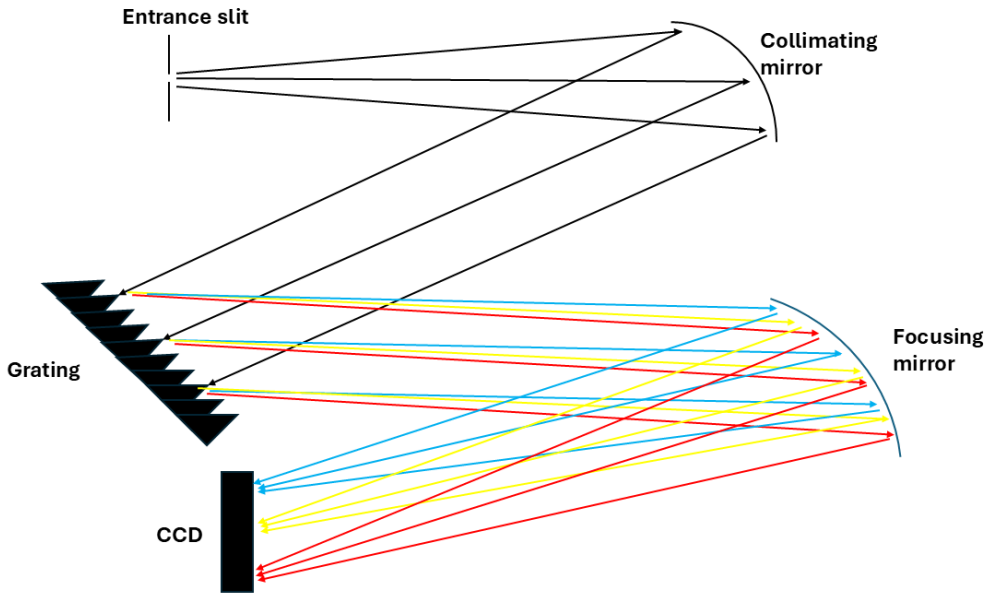

Figure 2.3: Schematic of a spectrometer with Czerny-Turner configuration

The light enters the spectrometer through the entrance slit and then hits the collimating mirror, which produces a parallel light beam. The light is then separated depending on wavelength by the reflective grating, following the grating equation:

$$\mathrm{a}(\sin(\theta_\mathrm{i}) - \sin(\theta_\mathrm{m})) = \mathrm{m}\lambda \tag{2.7}$$

Where a is the distance between the grooves, θ_i is the angle of the incident light beam, θ_m is the angle of the reflected light beam, m is the order of principal maxima and λ is the wavelength (see Figure 2.4) [10]. The light is then focused by the second concave mirror and directed to the CCD.

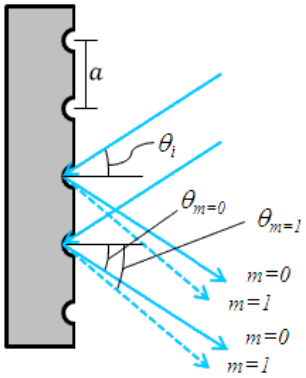

Figure 2.4: Schematic of a reflective grating [10]

2.3.2 Functional Principle of a Charge-Coupled Device

CCDs are integrated circuits, invented in 1969 by Willard Boyle and Goerge E. Smith. A CCD consists of a planar array of light-sensitive elements that convert photons into electrical charge. Each of these elements represents one pixel and is implemented by metal-oxide semiconductor capacitors (MOSCAP) etched into a semiconductor surface [11].

The MOSCAPs consist of a polysilicon gate and a silicon dioxide (SiO_2) insulator thin film, placed on top of a semiconductor substrate. For CCDs p-doped silicon is used as the substrate. Hence, it is referred to as an nMOS capacitor [11].

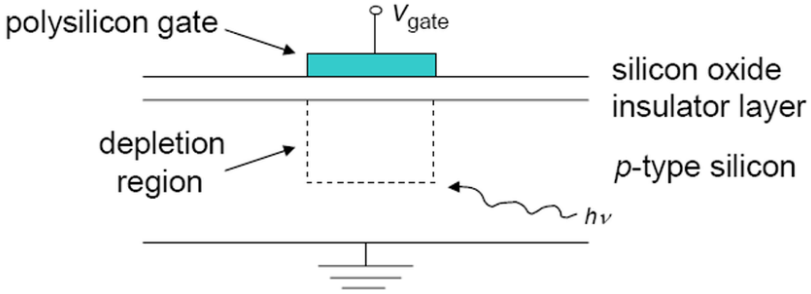

Figure 2.5: Metal-Oxide semiconductor capacitor [11]

When a positive voltage is applied to the gate, a depletion region is formed. If a photon with an energy higher than the semiconductors band gap hits the depletion zone, an electron-hole pair is created [[12]]. The electron is trapped in the depletion zone. The collected charge is proportional to the incident light. After the accumulation of charge, the CCD is read out row by row by applying alternating voltages to the electrodes. In that way, each column is shifted to the readout register one after another. From that register, one charge packet at a time is transferred to an output amplifier where it is converted to voltage which is then digitized and can be mapped to the respective pixel [13]. The readout process can be seen in Figure 2.6.

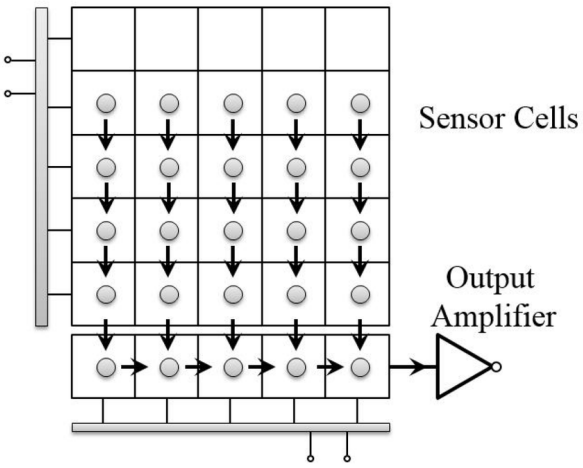

Figure 2.6: Readout process of a CCD [14]

A CCD can be characterized by multiple parameters. These parameters are the quantum efficiency, i.e. the percentage of photons that are detected, the wavelength range, the dynamic range, i.e. the range between the minimum and maximum of electrons that can be imaged, linearity and noise. Different forms of noise include readout noise and dark current [13].

2.3.3 Differential Optical Absorption Spectroscopy

The foundation for Differential Optical Absorption Spectroscopy (DOAS) is laid by Lambert-Beer's law, which was first formulated by Pierre Bouguer in 1729, later formalized by Johann Heinrich Lambert in 1760, and extended by August Beer in 1852 [2]. The law describes the decrease of light intensity when it passes through a medium of a certain length as a result of absorption. It is given by the following equation:

$$\mathrm{I}(\lambda) = \mathrm{I}_0(\lambda) \cdot \exp\left(- \sigma(\lambda) \cdot \rho \cdot \mathrm{s} \right) \tag{2.8}$$

Where $I(\lambda)$ is the intensity of the light after passing through the medium, $I_0(\lambda)$ is the initial intensity, $\sigma(\lambda)$ is the absorption cross section of a species, ρ is its concentration and s is the length of the light path through the absorbing medium. In the atmosphere, the intensity is altered not only by absorption by the target species but also by absorption by other species and scattering, especially Mie- and Rayleigh scattering [2] and surface reflectance and the presence of clouds, which is represented by the efficiency factor c [15]. To account for these aspects and the atmosphere's inhomogeneity, Equation 2.8 is augmented to

$$\begin{aligned} \mathrm{I}(\lambda) = c \cdot I_0(\lambda) \cdot \exp\Bigg(- \int_0^s \Bigg[& \sum_{j=1}^{J} \sigma_j(\lambda) \cdot \rho_j(s') \\ & + \sigma_{\mathrm{Ray}}(\lambda) \cdot \rho_{\mathrm{Ray}}(s') + \sigma_{\mathrm{Mie}}(\lambda) \cdot \rho_{\mathrm{Mie}}(s') \Bigg] ds' \Bigg) \end{aligned} \tag{2.9}$$

with σ_{Ray} and σ_{Mie} being the Rayleigh- and Mie extinction cross sections and ρ_{Ray} and ρ_{Mie} being the concentrations of Mie- and Rayleigh scattering particles. The slant column density is defined as

$$\mathrm{SCD} = \int_0^{\mathrm{s}} \rho(\mathrm{s}')\mathrm{ds}' \tag{2.10}$$

This definition can be inserted into Equation 2.9, leading to the following equation.

$$\begin{aligned} \mathrm{I}(\lambda) = c \cdot I_0(\lambda) \cdot \exp\Bigg(& - \sum_{j=1}^{J} \sigma_j(\lambda) \cdot SCD_j \\ & - \sigma_{\mathrm{Ray}}(\lambda) \cdot SCD_{\mathrm{Ray}} - \sigma_{\mathrm{Mie}}(\lambda) \cdot SCD_{\mathrm{Mie}} \Bigg) \end{aligned} \tag{2.11}$$

The target slant column densities are now retrieved with the DOAS method with the basic notion of dividing the signal into quickly and slowly varying components. From the fast-varying part the

atmospheric absorptions are acquired, and the slowly varying component is approximated by a low order polynomial [15]. The separation into high and low frequency components is represented by the following equation:

$$\sigma(\lambda) = \sigma^*(\lambda) + \sigma'(\lambda) \tag{2.12}$$

where $\sigma^*(\lambda)$ is the slowly varying component and $\sigma'(\lambda)$ is the fast-varying component of the absorption cross-section. This separation is only possible for absorbers with structured absorption spectra, and therefore not for Rayleigh and Mie scattering processes. When applying this idea to Equation 2.11, the following equation is yielded:

$$\begin{aligned} \mathrm{I}(\lambda) = c \cdot I_0(\lambda) \cdot \exp\Bigg(&- \sum_{j=1}^{J} \sigma'_j(\lambda) \cdot SCD_j - \sum_{j=1}^{J} \sigma^*_j(\lambda) \cdot SCD_j \\ &- \sigma_{\mathrm{Ray}}(\lambda) \cdot SCD_{\mathrm{Ray}} - \sigma_{\mathrm{Mie}}(\lambda) \cdot SCD_{\mathrm{Mie}} \Bigg) \end{aligned} \tag{2.13}$$

The low frequency component is combined with the Mie- and Rayleigh scattering cross sections and approximated by a polynomial:

$$\mathrm{I}(\lambda) = c \cdot I_0(\lambda) \cdot \exp\left(- \sum_{j=1}^{J} \sigma'_j(\lambda) \cdot SCD_j - \sum_{p=1}^{P} a_p \lambda^p \right) \tag{2.14}$$

When expressed in terms of optical depth $OD = \ln \frac{I_0}{I}$, Equation 2.14 reads as the so-called DOAS equation:

$$\mathrm{OD} = \ln \frac{\mathrm{I_0}}{\mathrm{I}} = \sum_{\mathrm{j=1}}^{\mathrm{J}} \sigma'_{\mathrm{j}}(\lambda) \cdot \mathrm{SCD_j} + \sum_{\mathrm{p=0}}^{\mathrm{P}} \mathrm{c_p} \lambda^{\mathrm{p}} \tag{2.15}$$

The factor c, which was introduced in Equation 2.9 is now also included in the polynomial for the slowly varying components. The optical depth is the measured signal. The equation is set up for each measured wavelength, resulting in a system of linear equations, which is then solved with a least squares algorithm, which yields the slant column densities of the target species [15]. In order to be a target species for DOAS measurements, trace gases need distinct narrow band absorption structures. Typical gases retrieved with the DOAS technique are for example NO_2, SO_2 or O_3 [2].

Usually, the desired result of DOAS measurements is the vertical trace gas column density (VCD), that is, the concentration of trace gases vertically integrated over the height of the atmosphere [2],

defined as:

$$\mathrm{VCD} = \int_0^{\mathrm{z}} \rho(\mathrm{z}')\mathrm{dz}' \tag{2.16}$$

The vertical column density is linked to the slant column density by the air mass factor (AMF):

$$\mathrm{AMF} = \frac{\mathrm{SCD}}{\mathrm{VCD}} \tag{2.17}$$

In scenarios with simple light paths, where scattering does not play a significant role (e.g. direct-sun DOAS) and effects of Earth's curvature and refraction in the atmosphere are negligible, the air mass factor can be calculated as:

$$\mathrm{AMF} \approx \frac{1}{\cos(\theta)} \tag{2.18}$$

where θ is the solar zenith angle. For viewing geometries that rely on scattered light, this geometric approach is no longer valid, but it remains a good approximation for solar zenith angles up to 75° [2]. In such cases, detailed radiative transfer models are employed to obtain a more accurate air mass factor.

In practice, the light is focused on a CCD detector by a spectrometer, to record the spectrum. The instrument has a limited resolution and, therefore, alters the shape of the spectrum. This alteration is described by a convolution of the light intensity $I(\lambda, s)$ with an instrument function H:

$$\mathrm{I}^*(\lambda, \mathrm{s}) = \mathrm{I}(\lambda, \mathrm{s}) * \mathrm{H} = \int \mathrm{I}(\lambda - \lambda', \mathrm{s}) \cdot \mathrm{H}(\lambda')\mathrm{d}\lambda' \tag{2.19}$$

The changed spectrum is then projected on the detector array, where the intensity is discretized:

$$\mathrm{I}'(\mathrm{i}) = \int_{\lambda(\mathrm{i})}^{\lambda(\mathrm{i}+1)} \mathrm{I}^*(\lambda, \mathrm{s})\mathrm{d}\lambda' \tag{2.20}$$

with i being the number of the pixel. The wavelength-pixel-mapping in the case of a perfect linear dispersion is described as:

$$\lambda(\mathrm{i}) = \gamma_0 + \gamma_1 \times \mathrm{i} \tag{2.21}$$

In practice, the dispersion is not linear. Therefore, it is approximated as a polynomial:

$$\lambda(\mathrm{i}) = \sum_{\mathrm{k}=0}^{\mathrm{q}} \gamma_{\mathrm{k}} \cdot \mathrm{i}^{\mathrm{k}} \tag{2.22}$$

where γ_k are polynomial coefficients which form the parameter vector $\boldsymbol{\gamma}$ that describes the wavelength-

pixel-mapping. γ_0 represents a spectral shift, and γ_1 represents linear scaling (i.e., squeezing or stretching), γ_k with higher values of k represent higher order distortions. The parameter vector is influenced by changes in measurement conditions. In this thesis, the alteration of the measurement conditions due to variations in the spectrometer temperature plays a prominent role, as these fluctuations primarily impact γ_0. Therefore, they produce a shift in the measured spectra [2]. This shift can be mitigated by stabilizing the spectrometer temperature.

In this thesis, ground-based passive DOAS will be used. That means that, in contrast to active DOAS applications, only light from a natural source (in this case the sun) will be utilized. In passive DOAS the light path is determined by the position of the sun, the viewing direction of the telescope, and scattering of light by air molecules and aerosols [2]. In passive DOAS multiple viewing geometries are often employed, each measuring a different light path and, hence, probe different atmospheric layers. Three of the most commonly used geometries are explained below.

Direct-Sun DOAS

As indicated by the name, the telescope is directly pointed at the sun for the direct-sun technique (Figure 2.7). This viewing geometry is sensitive to tropospheric as well as stratospheric absorptions [16]. In this geometry the light path can be assumed as well defined, as scattered light does not have a large influence. Therefore, there is only a small uncertainty in AMF.

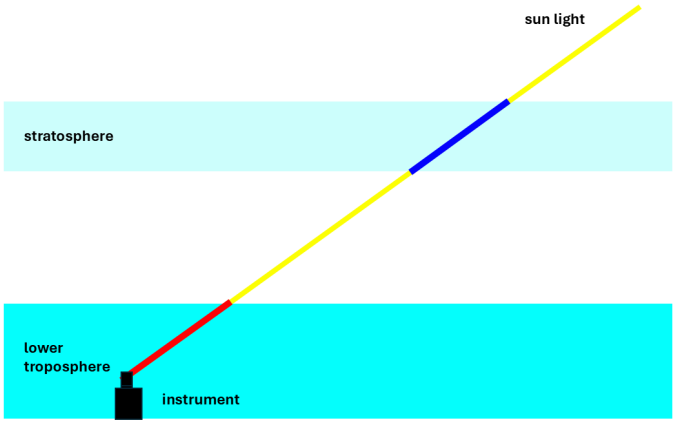

Figure 2.7: Direct-Sun DOAS viewing geometry, adapted from [17]

Zenith-Sky DOAS

The zenith-sky viewing geometry is useful for stratospheric observations. In this geometry the light path in the lower troposphere remains the same. The light path in the stratosphere is determined by the position of the sun and scattering. As the light path is the longest during twilight, the sensitivity

of zenith-sky DOAS measurements is the highest during dusk and dawn. Usually data are compared between twilight measurements and a reference measurement around noon. Assuming a constant tropospheric light path and concentrations, its contribution to the measurement cancels out [17].

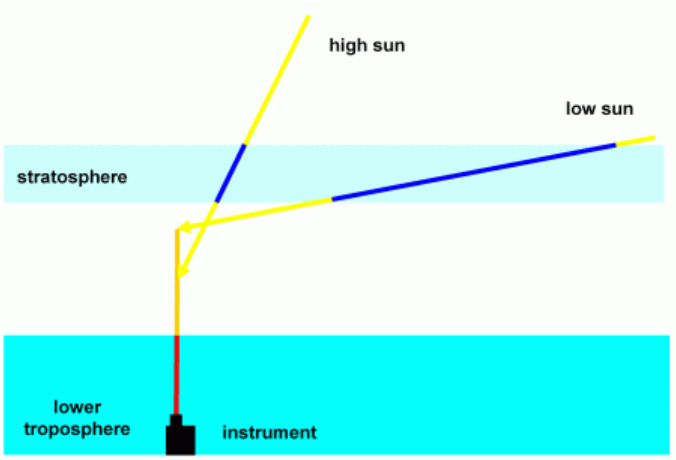

Figure 2.8: Zenith-Sky DOAS viewing geometry [17]

Multi-Axis DOAS

For multi-axis DOAS (MAX-DOAS) scattered light is measured under various viewing elevation angles from horizon level to zenith. The length of the light path through the lower troposphere depends on these elevation angles and the mean free path of the photon [17], i.e., the presence of aerosols and other scattering particles determining the final scattering point. A zenith-sky measurement is taken as a reference spectrum. The light path in the stratosphere is assumed to be independent of the elevation angle. Hence, stratospheric contributions cancel out making MAX-DOAS viable for measuring tropospheric absorbers [16].

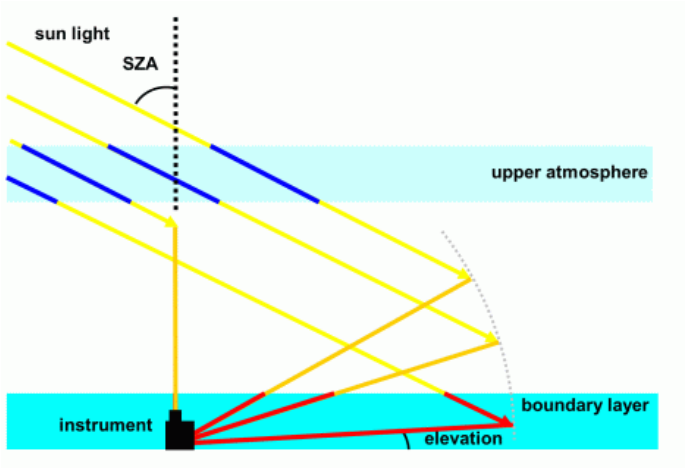

Figure 2.9: Multi-Axis DOAS viewing geometry [17]

2.4 Functional Principle of a Peltier Element

In this thesis, thermoelectric phenomena are used for the thermal control of the measurement system. One basic effect of thermoelectricity is the Seebeck effect, that was first discovered by Alessandro Volta in 1774 and then independently discovered by and named after Thomas Seebeck in 1821 [18]. Volta and Seebeck discovered that a voltage difference is generated when two dissimilar materials form junctions that are kept at different temperatures. The reason for this is the flow of electrons along the temperature gradient due to kinematic agitation. The generated voltage is described by the following equation (see Figure 2.10A):

$$\mathrm{V} = \Delta\mathrm{T} \cdot (\mathrm{S_B} - \mathrm{S_A}) \tag{2.23}$$

With ΔT being the temperature difference between the junctions, and S_A and S_B being the Seebeck coefficients of materials A and B respectively. Often, semiconducting materials are chosen for their favorable Seebeck coefficients. One example of utilization of the Seebeck effect are thermocouples that are used to measure temperature. A schematic of the effect can be seen in Figure 2.10B.

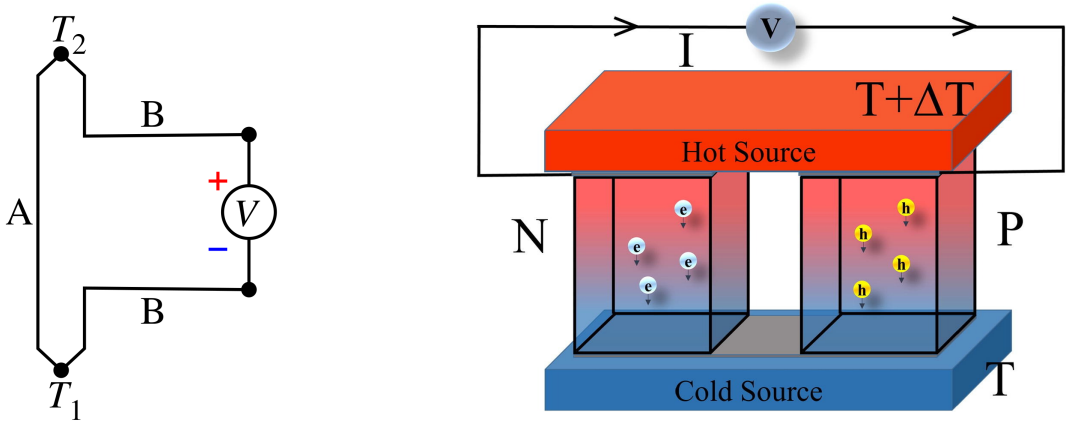

(a) Simplified electric circuit representation of the Seebeck effect [19]

(b) Schematic illustration of charge carrier movement leading to a voltage difference across a temperature gradient [18]

Figure 2.10: Principle of the Seebeck Effect

The Peltier effect can be understood as the reverse of the Seebeck effect. It was discovered by the French physicist Jean Charles Athanase Peltier in 1834. When current is driven through such a circuit, one junction dissipates heat, while the other absorbs it. The heat flow $\dot{Q}$ through a junction between two materials is computed by

$$\dot{\mathrm{Q}} = (\Pi_{\mathrm{A}} - \Pi_{\mathrm{B}}) \cdot \mathrm{I} \tag{2.24}$$

where Π_A and Π_B are the Peltier coefficients of the materials, representing the amount of heat transported per unit charge, and I is the current from A to B [20]. The resulting heat does not only depend on the Peltier effect, but also on Joule heating, i.e., the heat dissipated as a result of a current flowing through a conductor. A typical thermoelectric module (TEM) consists of multiple of those elements, connected electrically in series and thermally in parallel [21].

2.5 PID Temperature Control

To achieve a constant temperature within the measurement system, it is essential to set up a precise temperature control. In general, the objective of any control is to force a system to a desired behavior, i.e., to bring the controlled variable (x) to a certain setpoint (w) by setting a manipulated variable (y).

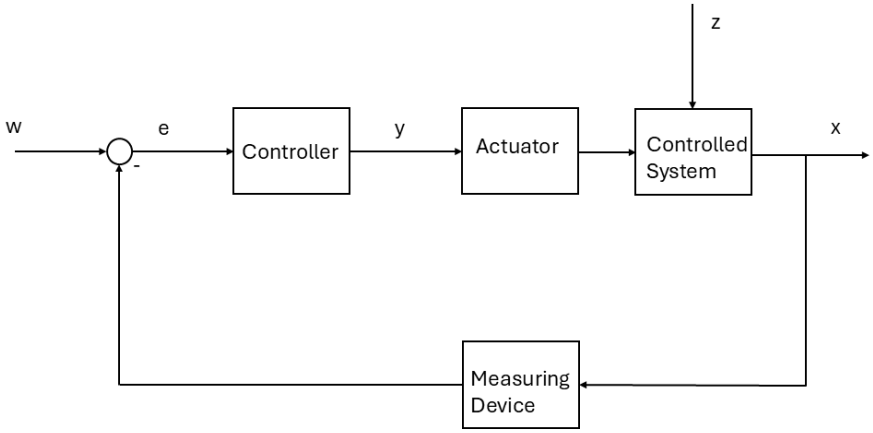

Figure 2.11: Elements of a control loop [22]

As shown in Figure 2.11, the control loop consists of a controller, an actuator, the controlled system itself, and a feedback with a measuring device. The input to the controller is the error, which is given by the following equation [22].

$$e = w - x \tag{2.25}$$

That means that the controlled variable is continuously measured, fed back, and compared to the setpoint. The controller then sets the manipulated variable to eliminate the deviation between the controlled variable and the setpoint. According to the manipulated variable, which is a digital signal, the actuator changes the actual physical output to influence the controlled system. In the case of this thesis, the controlled variable is the temperature inside the instrument box, the setpoint is the desired temperature, the manipulated variable is a low-power signal of the necessary power fed to the TEM and the actuator is a power converter (pulse width modulation) that controls the TEM's input.

The utilized PR59-Controller provides a PID-controller. As given by its name, the PID-controller consists of the following three components:

- proportional action (P-component)
- integral action (I-component)
- derivative action (D-component)

The controller output (i.e. the manipulated variable) is given by:

$$\mathrm{y(t)} = \mathrm{K_P} \cdot \mathrm{e(t)} + \mathrm{K_I} \cdot \int_0^{\mathrm{t}} \mathrm{e}(\tau)\,\mathrm{d}\tau + \mathrm{K_D} \cdot \frac{\mathrm{d}}{\mathrm{dt}}\,\mathrm{e(t)} \tag{2.26}$$

Equation 2.26 shows that the P-component reacts as soon as an error occurs and multiplies it by the gain K_P. It brings the controlled variable near to the setpoint, but is not capable of completely eliminating the error. The I-component integrates the error over time and multiplies it by the constant K_I. The I-component leads to the error becoming zero. The D-component takes the derivative of the error over time. That means that it quickly reacts to changes and, therefore, improves the dynamic of the control system.

3. Setup of the Measurement System

The measurement system consists of an aluminum box with inner dimensions of 750 mm × 550 mm × 380 mm ($L \times W \times H$), which is equipped with a TEM protected against precipitation by a rain shield, a GNSS antenna for positioning, an LTE antenna for mobile broadband communication, and cable connections. The interior of the box is thermally insulated with 40 mm of styrodur and accommodates a measurement computer, a spectrometer, as well as power supplies for the TEM, the computer, the pan-tilt head and a calibration lamp. The complete outer setup is shown in Figure 3.1.

Figure 3.1: Complete box, including TEM, cable connectors, antennas and rain shield

3.1 Design Specifications

The design process was guided by a set of specifications, which were defined considering the fields of use of the measurement system and are summarized as follows:

- **Temperature stability:** The system is intended to be used in both hot and cold environments. Therefore, it needs to be equipped with a thermoelectric module (TEM) that is capable of providing enough heating and cooling power and must be thermally insulated.
- **Flexibility:** There are two different use cases of the measurement system. The first one is an outdoor application, where the system contains the smaller Avantes spectrometer and all accessory components (see Section 3.3). The second use case is an indoor application, where only the bigger Princeton Instruments SP2300 spectrometer with the CCD detector is placed within the box and the accessory components are placed in the laboratory.
- **Environmental protection:** As the system is used in outdoor applications, it needs to be protected against precipitation. A rain shield for the TEM and waterproof components must be utilized.
- **Ease of use:** The system will possibly be employed on measurement campaigns. Hence, it must be transportable and quick and straightforward to set up under unfavorable environmental conditions.

3.2 Heat Load Estimation

The choice of the TEM is determined by spatial restrictions, the cooling power that needs to be provided, and its suitability for the outdoor use case. The required cooling power depends on the heat dissipated from the devices inside the box and the heat transfer from outside under conditions when the ambient temperature is higher than the control temperature. The heat transfer from the outside into the box is described as follows.

$$\dot{\mathrm{Q}} = \frac{\Delta \mathrm{T}}{\sum \mathrm{R_{th}}} \tag{3.1}$$

with ΔT being the temperature difference between inside and outside the box and R_{th} the thermal resistance, calculated by:

$$\mathrm{R_{th}} = \frac{\delta}{\lambda \cdot \mathrm{A}} \tag{3.2}$$

where δ denotes the thickness of the material that conducts the heat, λ is its thermal conductivity, and A denotes the surface. In an approximation the outer surface of the styrodur insulation inside the aluminum box is taken for A. The thermal resistance of the aluminum box itself is neglected as $\lambda_{\text{Alu}} \gg \lambda_{\text{Styr}}$. Heat transfer due to leakages is neglected as well. With these approximations the thermal conductivity and the surface are estimated as $\lambda = 0.034\,\text{W/mK}$ and $A = 1.5\,\text{m}^2$. The thickness of the insulation is $\delta = 0.04\,\text{m}$. The heat transfer depending on the temperature difference is shown in Figure 3.2.

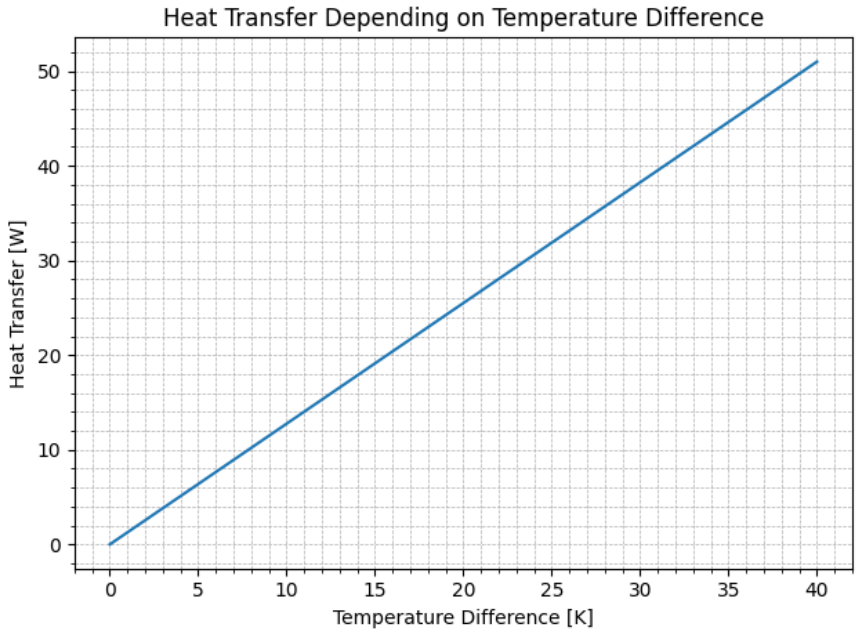

Figure 3.2: Heat transfer into the box depending on temperature difference between inside and outside the box

Heat sources are the notebook computer and the power supplies of the accessory devices (see Section 3.3). The heat dissipated from the computer is estimated to be $Q_{\text{PC}} = 15\,\text{W}$ as there is a constant load by gathering measurement data, but the display is turned off at all times, reducing heat dissipation. As the HgCd calibration lamp is not operated during normal measurements, any heat dissipated by its power supply can be neglected. The TEM AA-150-24-44 by Tark Thermal Solutions is the most favorable module because it is the most powerful TEM with appropriate dimensions and IP54 protection degree rating. The maximum power required by the preferred TEM is estimated to be $P_{\text{in}} = 190\,\text{W}$ [23]. Given that the efficiency of the power supply is $\eta = 0.85$ the maximum heat dissipated by the power supply is equal to its lost power, which is approximately $Q_{\text{TEM}} = 190\,\text{W}\left(\frac{1}{0.85} - 1\right) = 33.5\,\text{W}$. The heat dissipation from the pan-tilt head power supply is estimated to be $Q_{\text{PTH}} = 10\,\text{W}$. Thus, the total heat that needs to be compensated is as follows:

$$\mathrm{Q_{tot}} = \mathrm{Q_{PC}} + \mathrm{Q_{TEM}} + \mathrm{Q_{PTH}} + \dot{\mathrm{Q}} \tag{3.3}$$

The required cooling power Q_C depending on temperature difference and including a safety margin of 20 % to compensate for flawed estimations and uncertainties computes to:

$$\mathrm{Q_C} = 1.2(58.5\,\mathrm{W} + \dot{\mathrm{Q}}(\Delta\mathrm{T})) \tag{3.4}$$

Figure 3.3 shows the estimated heat load and the cooling power of the preferred TEM. It can be inferred from the interception of both curves that the TEM can stabilize the temperature within the box for a temperature difference of up to 15 K between the ambient temperature and the control temperature, which is sufficient for all use cases.

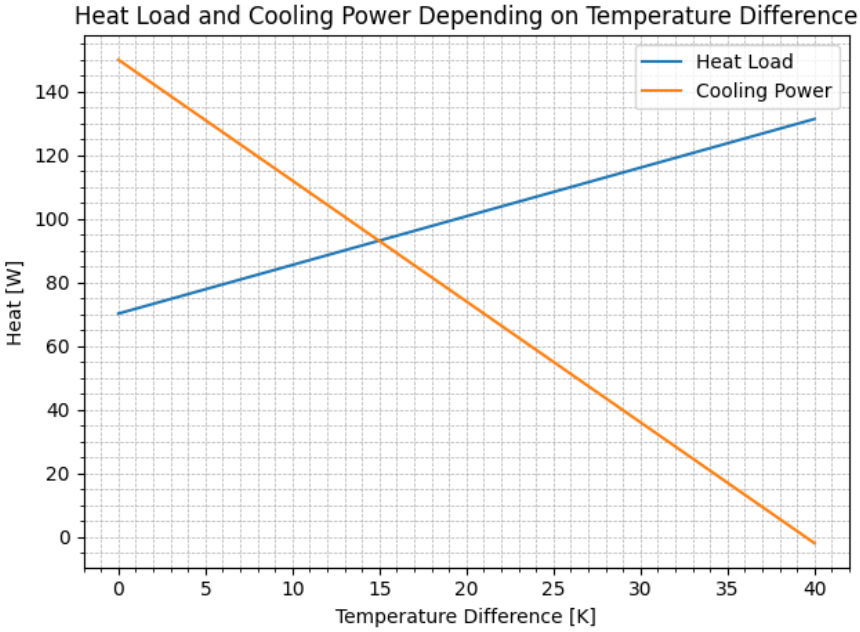

Figure 3.3: Heat load including a safety margin of 20 % and AA-150-24-44 TEM cooling power depending on temperature difference

If the heat loss through the insulation exceeds the internally dissipated heat, the TEM must supply heating power. The temperature difference for the heating case is calculated as follows from Equations 3.1 and 3.2:

$$\Delta\mathrm{T} < -\mathrm{Q_{diss}}\mathrm{R_{th}} \tag{3.5}$$

Where $Q_{\mathrm{diss}} = Q_{\mathrm{PC}} + Q_{\mathrm{PTH}}$ denotes the combined heat dissipation of the computer and the pan-tilt

head power supply. The TEM's own dissipation is omitted since it is inactive in this boundary case. Substituting the values yields a threshold of $\Delta T < -19.6\,\mathrm{K}$, meaning that heating is required when the ambient temperature is 19.6 K colder than the set point.

3.3 Components

Thermoelectric Module

The TEM is the actuator of the temperature control. Based on the design specifications and cooling power estimates, discussed in Sections 3.1 and 3.2, the TEM AA-150-24-44 by Tark Thermal Solutions was chosen. It can be mounted to the housing and is equipped with high-density heat exchangers, that absorb or dissipate heat, and fans on the hot and cold sides to enable forced-air convection. It is rated with IP54 degree of protection. That means that it is protected against limited amounts of dust, and water sprays from all directions. The TEM is protected by an additional rain shield, making it suitable for outdoor applications. The maximum cooling power depends on the temperature difference between ambient and control temperature (see Figure 3.3). The maximum heating power also depends on the temperature difference, but is rated by the manufacturer at 150 W at an external temperature of $-40\,^{\circ}\mathrm{C}$ and a temperature difference of $45\,^{\circ}\mathrm{C}$ [23].

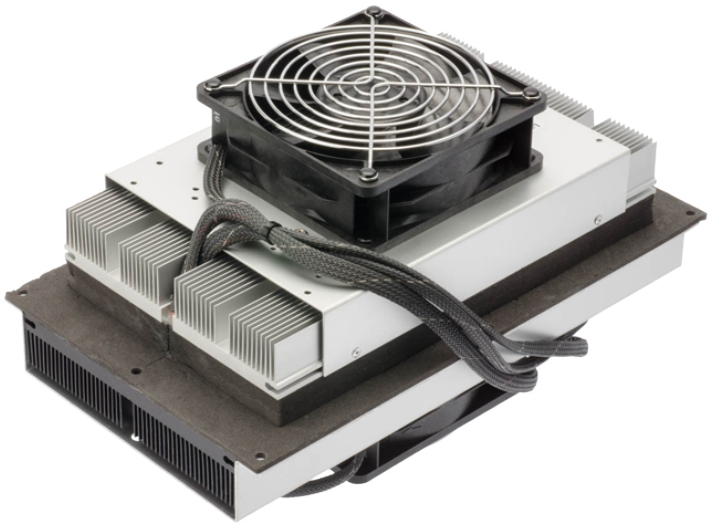

Figure 3.4: AA-150-24-44 Thermoelectric Module [23]

TEM Controller

The temperature control is realized with the TC-XX-PR-59 temperature controller from the same manufacturer. It provides an already implemented PID algorithm, a pulse-width-modulation (PWM) controlled TEM output, fan outputs as well as thermometer inputs, and an RS-232 interface for communication with the computer.

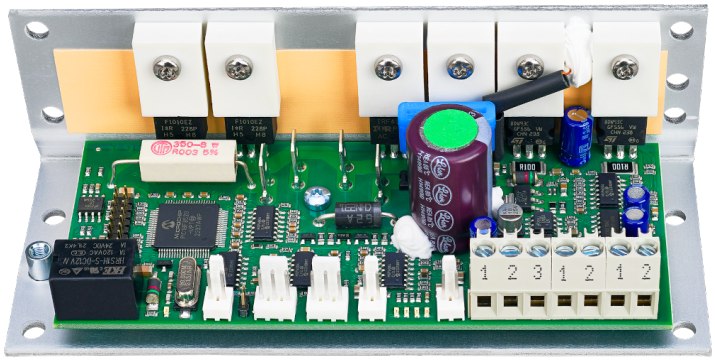

Figure 3.5: TC-XX-PR-59 temperature controller [24]

Avantes Spectrometer

The Avantes AvaSpec ULS2048x64 spectrometer is used in the measurement system. It is a Czerny-Turner spectrometer with a spectral range of 270 nm to 530 nm and a spectral resolution of 0.6 nm. The spectrometer is equipped with a back-thinned CCD detector. It was chosen for its high accuracy and small dimensions. The spectrometer is powered by the computer via USB.

Computer

A notebook computer hosts the measurement software and the software for the temperature controller setup. A Cleware USB-Humi 1.2 combined temperature and humidity sensor is connected to the computer for additional monitoring of conditions.

Antennas

A GNSS antenna facilitates positioning of the measurement system, and an LTE antenna enables internet connectivity when a wired network is not available. Both are connected to the measurement computer.

Power Converter for Pan-Tilt Head including ADAM Converter

The power converter supplies the pan-tilt head's motor with electrical power. The integrated ADAM converter enables the communication and control signals for precise positioning. Together, they facilitate the multi-axis alignment needed for MAX-DOAS measurements.

Power Converter for Calibration Lamp

The power converter supplies the mercury-cadmium (HgCd) calibration lamp, which is inside the telescope, with electrical power. The HgCd lamp emits distinct spectral lines at known wavelengths, which can be used for the wavelength calibration of the spectrometer.

3.4 Modifications of the Zarges Box

A Zarges K470 Universal Box with interior dimensions of 750 mm × 550 mm × 380 mm ($L \times W \times H$) served as the platform for the measurement system. The box needed to be modified to allow mounting of the TEM, the antennas, and an exchangeable cable entry and connection plate. All components were placed on the same side to guarantee accessibility to all components and an adequate air flow to the TEM when the measurement system is operated in confined spaces such as room corners or between other instruments. The component layout was determined by the TEM, which is the largest item with the most positioning constraints. The TEM was positioned to avoid interference with component inside the box, in both indoor and outdoor application configuration. In particular, the dimensions of the larger spectrometer for the laboratory configuration and the positions of a weld seam and a clasp were the deciding constraints.

As the outer surface of the box incorporates raised bosses (protruding features; see Image 3.6), it is too uneven for the TEM to be mounted directly. Therefore, an aluminum frame was constructed (see Appendix B) that is mounted from the inside and holds the TEM from the outside, allowing the bosses to be sealed and providing a flat surface for the installation of the TEM (see Figure 3.6).

The cable connection plate was also made of aluminum. It hosts connector jacks for the pan-tilt head cable, power entry, and the HgCd calibration lamp, as well as an RJ45 jack for wired Internet connectivity, a cable gland for the optical fiber, and an illuminated power switch. The HgCd lamp connector was unavailable at the time, but can be added later. Instead, it was temporarily replaced by a cable gland for a temperature sensor. All chosen connectors and cable glands have at least an IP65 protection degree, which gives sufficient protection against precipitation. The cable connection plate was placed in the lower third of the box to avoid free hanging cables. The antennas were mounted in feed-through openings in the upper third.

All components were fastened with A4 stainless steel bolts and nuts to avoid corrosion. Each bolt was individually sealed with silicon O-rings so that no water can enter. Surface-to-surface connections between the cable connector plate and the box, and between the montage frame, the TEM and the box were sealed with foam sheet.

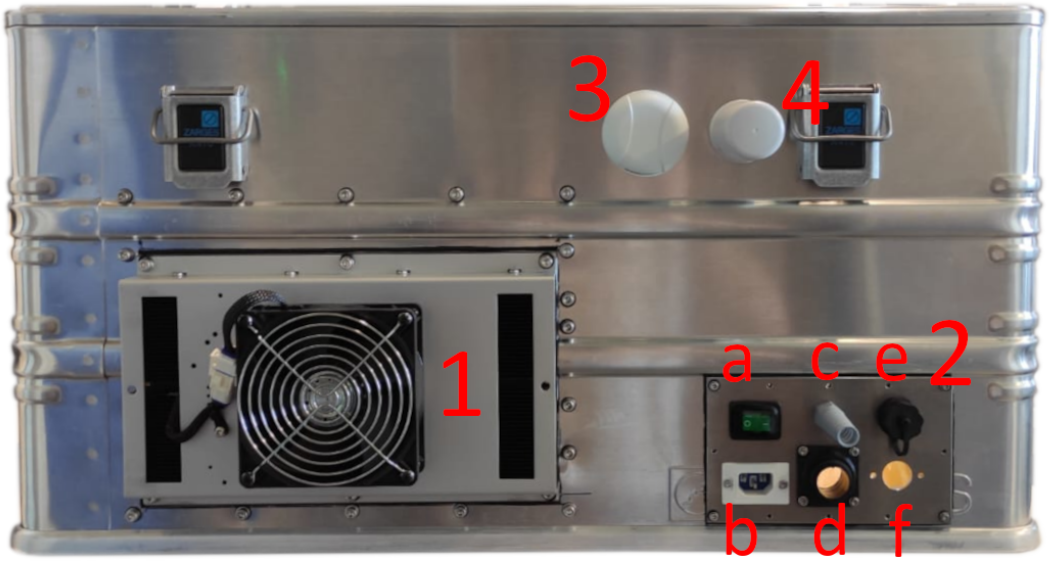

Figure 3.6: Modified Zarges Box with the components 1) TEM, 2) cable connector plate with a) power switch, b) power entry connector, c) cable gland for optical fiber, d) connector for pan-tilt head, e) RJ-45 jack, f) opening for HgCd lamp connector, 3) GNSS antenna, 4) LTE antenna

3.5 Interior Setup

The box accommodates the measurement computer with its power supply, the spectrometer, the power supply of the TEM and its controller and the pan-tilt head and HgCd lamp power converters. All devices are commercial end-user electronics that require an AC power supply (230 V, 50 Hz) using Schuko plugs (type-F). Therefore, a power strip is used for power distribution. The interior of the box is lined with 40 mm styrodur thermal insulation.

The combined footprint of the devices is too large to be accommodated on one single level. Hence, a two-level wooden rack was installed to hold the components. The devices are fastened for transport with hook-and-loop tape. The upper level is removable to allow access to the lower level if necessary. Power supplies and the TEM controller are placed at the lower level, and the computer and the spectrometer are placed at the upper level, as these components must be accessible for measurement setup and adjustment of the optical fiber. A schematic of both levels of the rack can be seen in Figure 3.7. The whole rack is clamped in place. The utilization of a rack has the advantage that the whole interior setup can quickly be removed, allowing for an easy switch between measurement configurations.

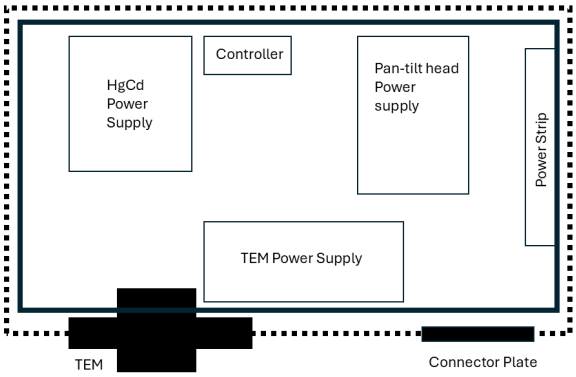

(a) Lower level with power supplies and TEM controller

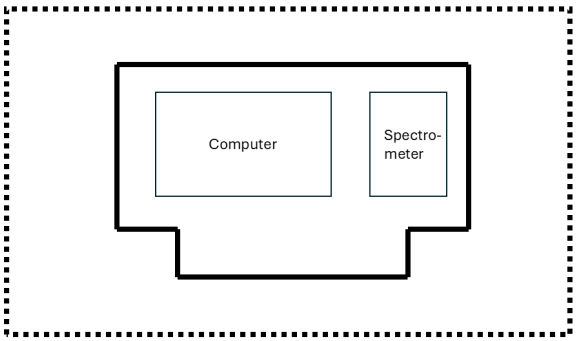

(b) Upper level with computer and spectrometer

Figure 3.7: Schematic of device arrangement on the rack (solid black lines). Outer boundaries of the box are depicted as a dotted line.

3.6 Controller Tuning

Although there are analytical controller tuning methods, an experimental approach was chosen to determine the control parameters as process testing was possible in the measurement system. This provided a quick and straightforward way to find PID tuning parameters.

To set a first reference point for the control parameter the tuning algorithm after Chien, Hrones and Reswick [25] was selected. For this method the step response of the open-loop-system is assessed by supplying the TEM with a step function of the manipulated variable, in this case a current value, and measuring the reaction of the temperature until a stable value is reached. The temperature is measured on the upper level of the wooden rack, next to the spectrometer. All components are installed in the box, but only the computer and the TEM, including its controller and power supply, are turned on.

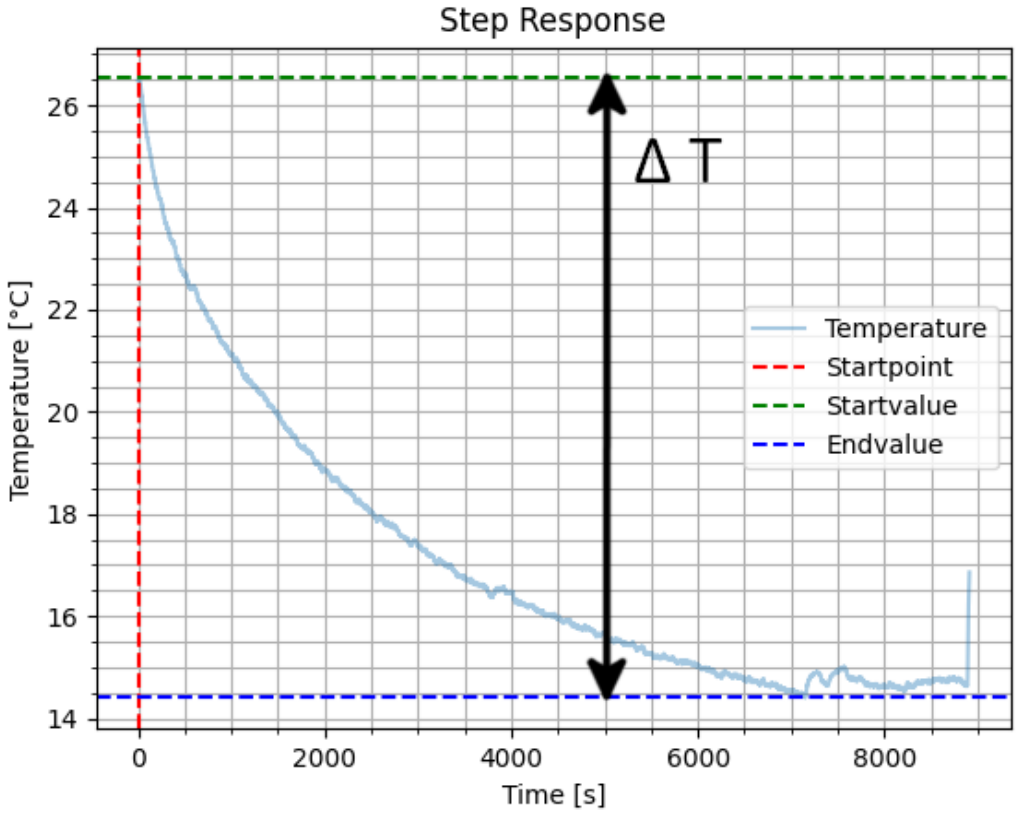

Figure 3.8: Step response of the measurement system

Figure 3.8 shows the step response of the system. The manipulated variable was set to $y_0 = -8.5\,\mathrm{A}$. The minimum of the controlled variable is $x_{\mathrm{end}} = 14.4\,^{\circ}\mathrm{C}$ and the maximum is $x_{\mathrm{start}} = 26.53\,^{\circ}\mathrm{C}$. The difference between the start and the final value is given by the following equation.

$$\Delta\,\mathrm{T} = \mathrm{k_S} \cdot \mathrm{y_0} = \mathrm{x_{end}} - \mathrm{x_{start}} \tag{3.6}$$

From Figure 3.8 it can be seen that $\Delta\,T = 12.13\,\mathrm{K}$. With Equation 3.6 it follows:

$$k_s = \frac{\Delta\,T}{y_0} = \frac{-12.13}{-8.5} = 1.43$$

Afterwards, the inflection tangent is drawn into the plot. From this tangent two further characteristics of the control loop can be seen.

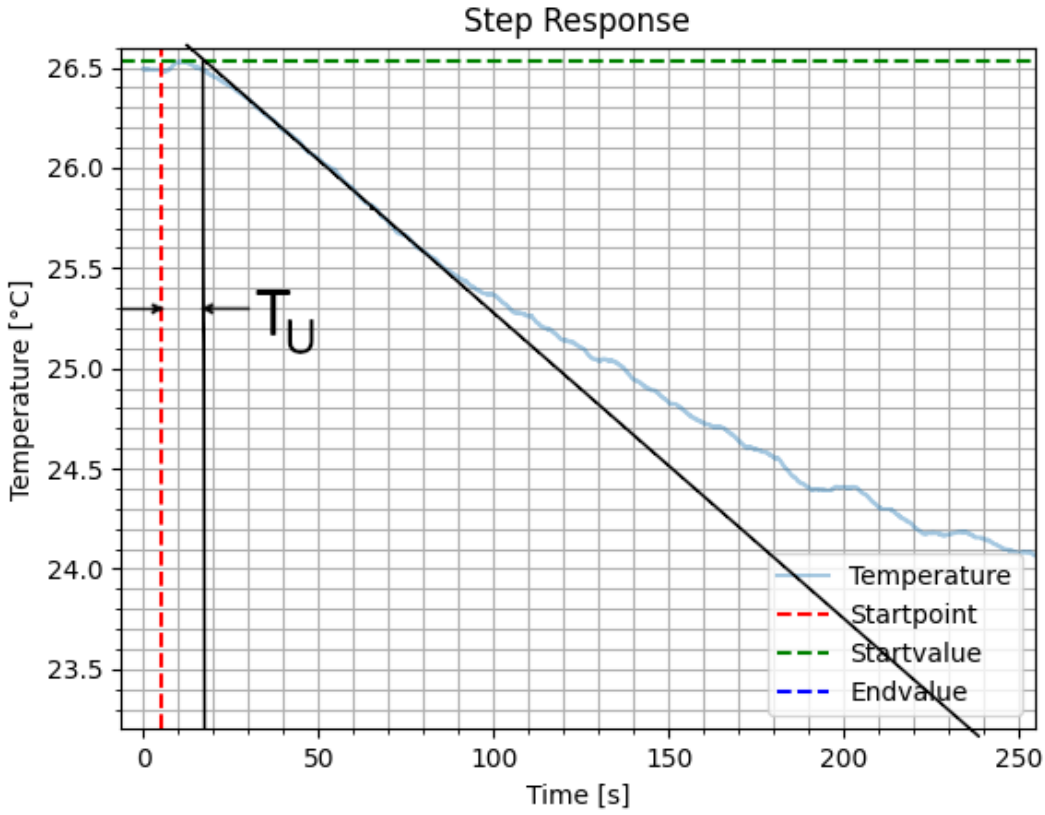

Figure 3.9: Step response with inflection tangent, first 250 s. The end value is not visible in this figure.

Figure 3.9 shows the first 250 s of the step response measurement with the inflection tangent. The time between the start point and the intersection of the inflection tangent with start value horizontal is called delay time T_U. The delay time is approximately $T_U = 10\,\text{s}$.

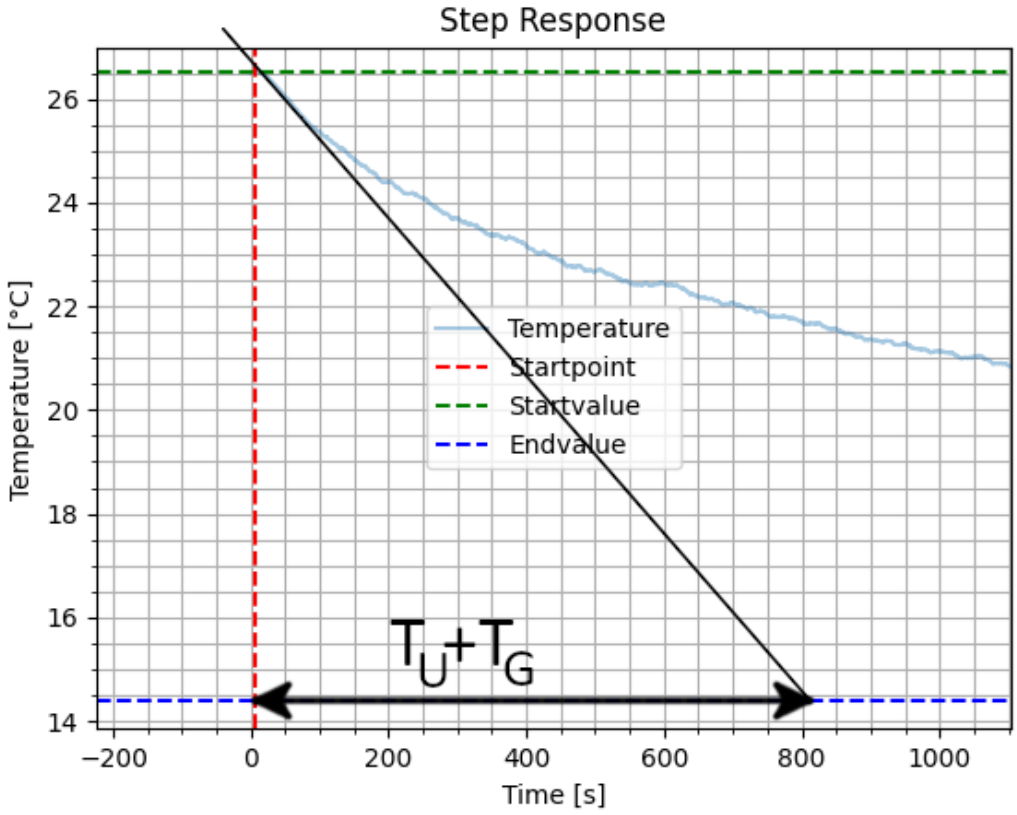

Figure 3.10: Step response with inflection tangent

In Figure 3.10 the first 1100 s of the step response can be seen. It shows the compensation time T_G. It is the time that elapses after the delay time until the inflection tangent crosses the horizontal at the final value. In this case, the compensation time is $T_G = 790\,\text{s}$.

With the parameters k_s, T_U and T_G the control loop can be tuned using the adjustment rules by Chien, Hrones and Reswick. This tuning technique was developed in 1952 and provides different tuning formulas depending on whether the goal is setpoint tracking or good mitigation of disturbances. Also either a fast regulation with approximately 20 % overshoot or a slower regulation with minimal or no overshoot can be chosen. The respective control parameters can be calculated using the formulas in the following table:

Table 3.1: Chien, Hrones and Reswick tuning for setpoint regulation and disturbance rejection [26]

Overshoot	**Controller**	**Disturbance Rejection**			**Setpoint Regulation**		
		K_R	T_N	T_V	K_R	T_N	T_V
Without Overshoot	P	$\frac{0,3}{K_S} \cdot \frac{T_G}{T_U}$	–	–	$\frac{0,3}{K_S} \cdot \frac{T_G}{T_U}$	–	–
	PI	$\frac{0,6}{K_S} \cdot \frac{T_G}{T_U}$	$4 \cdot T_U$	–	$\frac{0,35}{K_S} \cdot \frac{T_G}{T_U}$	$1,2 \cdot T_G$	–
	PID	$\frac{0,95}{K_S} \cdot \frac{T_G}{T_U}$	$2,4 \cdot T_U$	$0,42 \cdot T_U$	$\frac{0,6}{K_S} \cdot \frac{T_G}{T_U}$	T_G	$0,5 \cdot T_U$
With 20% Overshoot	P	$\frac{0,7}{K_S} \cdot \frac{T_G}{T_U}$	–	–	$\frac{0,7}{K_S} \cdot \frac{T_G}{T_U}$	–	–
	PI	$\frac{0,7}{K_S} \cdot \frac{T_G}{T_U}$	$2,3 \cdot T_U$	–	$\frac{0,6}{K_S} \cdot \frac{T_G}{T_U}$	T_G	–
	PID	$\frac{1,2}{K_S} \cdot \frac{T_G}{T_U}$	$2 \cdot T_U$	$0,42 \cdot T_U$	$\frac{0,95}{K_S} \cdot \frac{T_G}{T_U}$	$1,4 \cdot T_G$	$0,47 \cdot T_U$

$$K_I = \frac{K_R}{T_N} \quad ; \quad K_D = K_R \cdot T_V$$

As temperature processes are slow in general and, therefore, the high dynamic of the D action is not necessarily needed, a PI controller is chosen in the first approach. The tuning parameters were calculated using the formulas in Table 3.1 and can be found in the following table:

Table 3.2: Tuning parameters for a PI controller

Behavior	**Controller Type**	**Disturbance Rejection**			**Setpoint Regulation**		
		K_R	T_N	K_I	K_R	T_N	K_I
Without Overshoot	PI	33.14	40	0.8285	19.34	948	0.02
With 20% Overshoot	PI	38.67	23	1.68	33.14	790	0.042

The four tuning variants were tested afterwards. In the first measurements only the cooling capabilities of the control were tested. The starting temperature was 28 °C for all assessments. The setpoint was 20 °C.

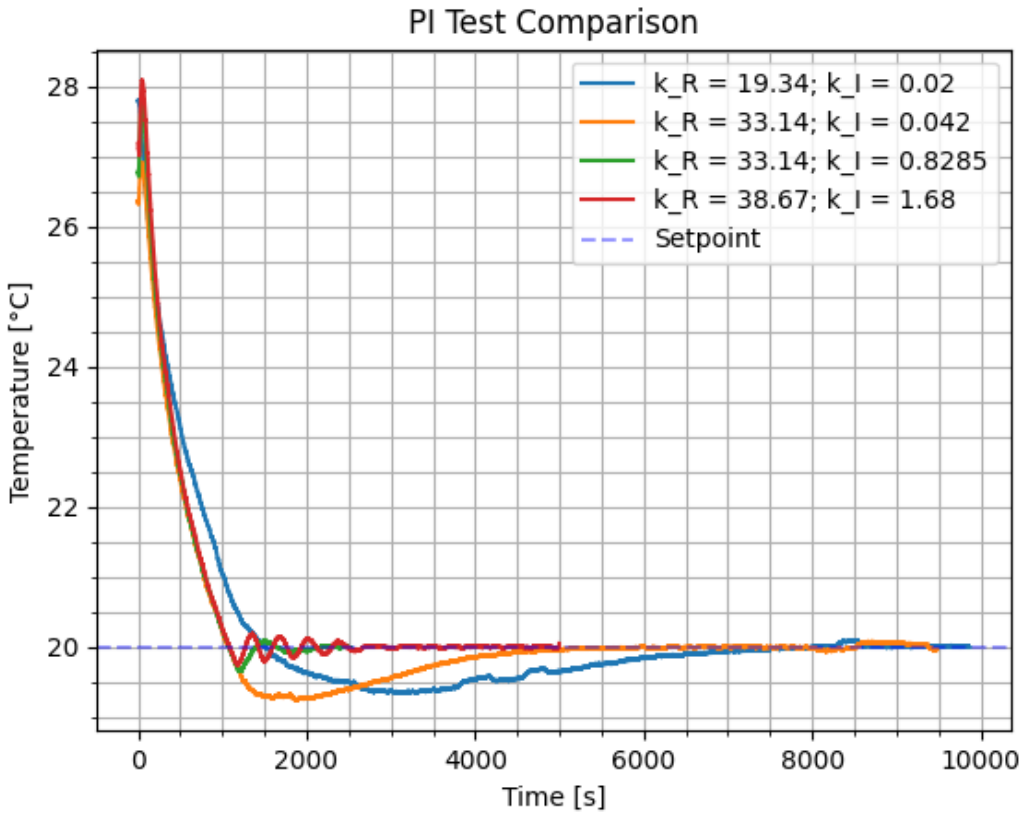

Figure 3.11: Comparison of four PI controller variants

Figure 3.11 shows the comparison of the four initial controller options. The blue curve represents the slower tuning, optimized for setpoint regulation. It can be seen that this controller tuning is very slow. It reaches the setpoint after roughly 2 h and has a small overshoot of 0.6 K or 7.5%, whereas the setpoint regulation optimized tuning variant with higher tolerance to overshoot, represented by the orange curve, does not show a significantly larger overshoot while having a settling time of only 1.5 h. The plot indicates that the tuning options, optimized for disturbance rejection, represented by the green and red curves, provide an even faster control with smaller overshoot and are therefore the preferred choices for further fine-tuning.

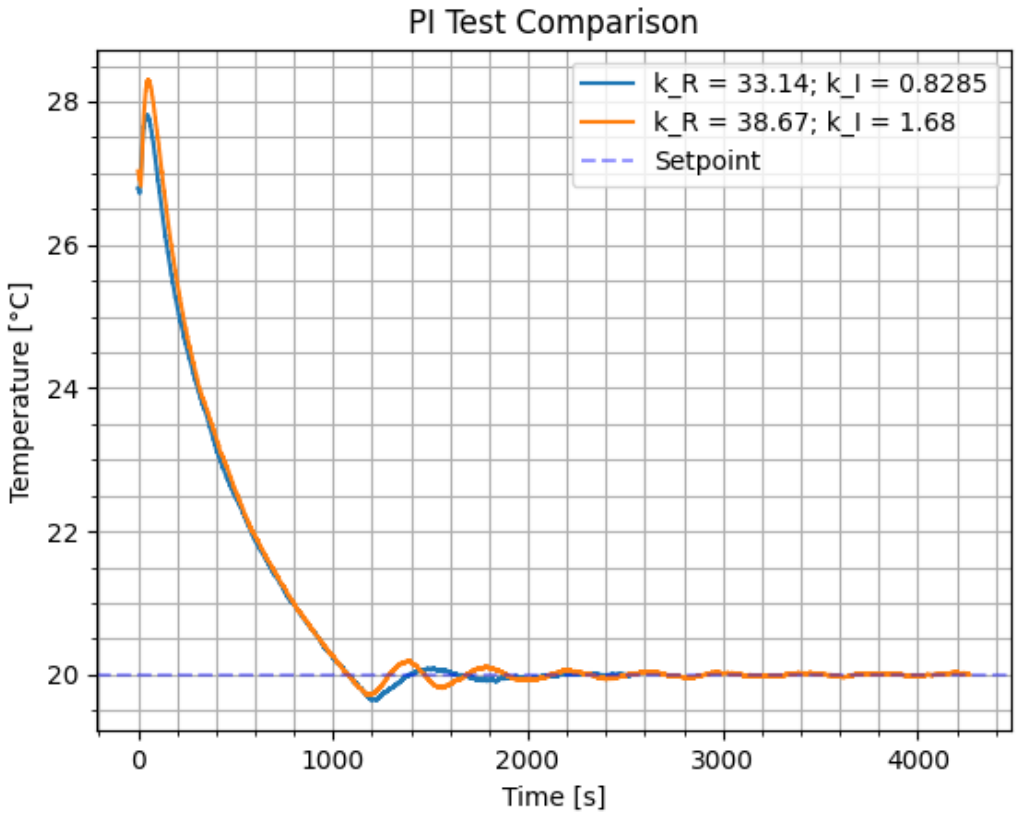

Figure 3.12: Comparison of disturbance rejection optimized PI controller variants

The comparison of the two variants optimized for disturbance rejection can be seen in Figure 3.12. Despite one variant being tuned with a bigger tolerance for overshoot, represented by the orange curve, and the other tuned for a small or no overshoot, in both cases the overshoot is approximately 0.5 K. The settling time for the tuning without overshoot is shorter, as the temperature for the other setting begins a dampened oscillation around the setpoint before eventually setting. Thus, the controller tuning without overshoot is chosen for further adaption.

In an attempt to improve the dynamics and reduce overshoot and settling time, the D-component was introduced and increased in small steps in a trial-and-error manner. The results of this iteration can be seen in Figure 3.13.

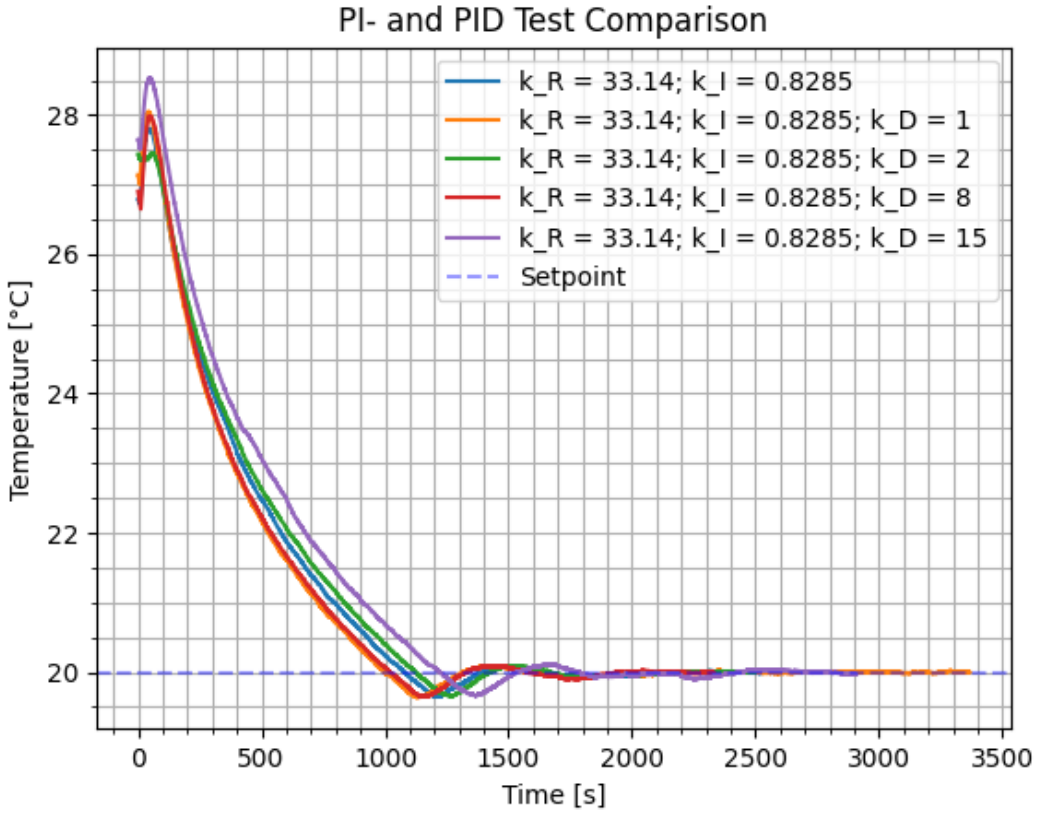

Figure 3.13: Comparison of PI and PID controller variants

It can be seen that the implementation of a D-component with a value of 8, represented by the red curve, slightly improved the control speed. For that reason, this tuning option was used as a starting point for adapting the controller to being capable of handling heating as well as cooling scenarios. The starting temperature for heating tests was 20 °C and the setpoint was 28 °C. With the initial settings, the temperature began to oscillate (see Figure 3.14, blue curve) and was therefore not usable.

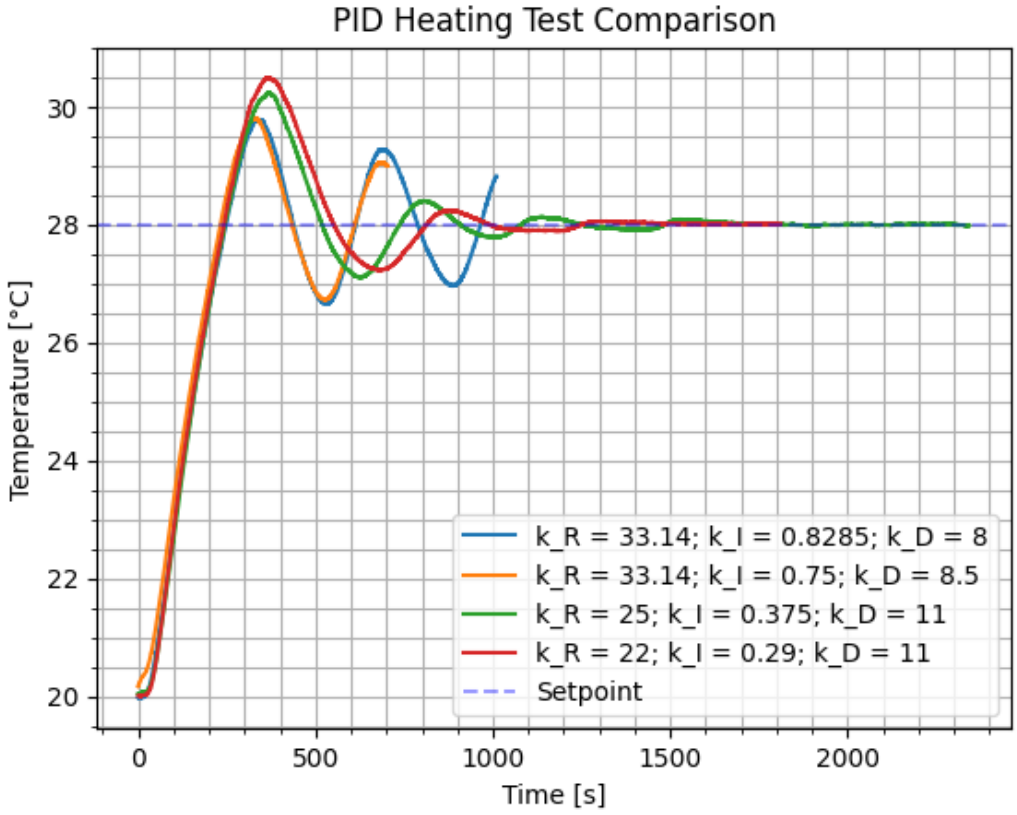

Figure 3.14: Comparison of PID controller variants in heating scenario

To improve control behavior, K_R and K_I were reduced, while K_D was increased iteratively. Afterwards, the tunings were also tested for the cooling scenario. These steps were repeated until a compromise was found between the ideal parameters for heating and cooling. Figure 3.15 shows the final choice of tuning parameters. The chosen parameters are $K_R = 22$, $K_I = 0.29$ and $K_D = 11$.

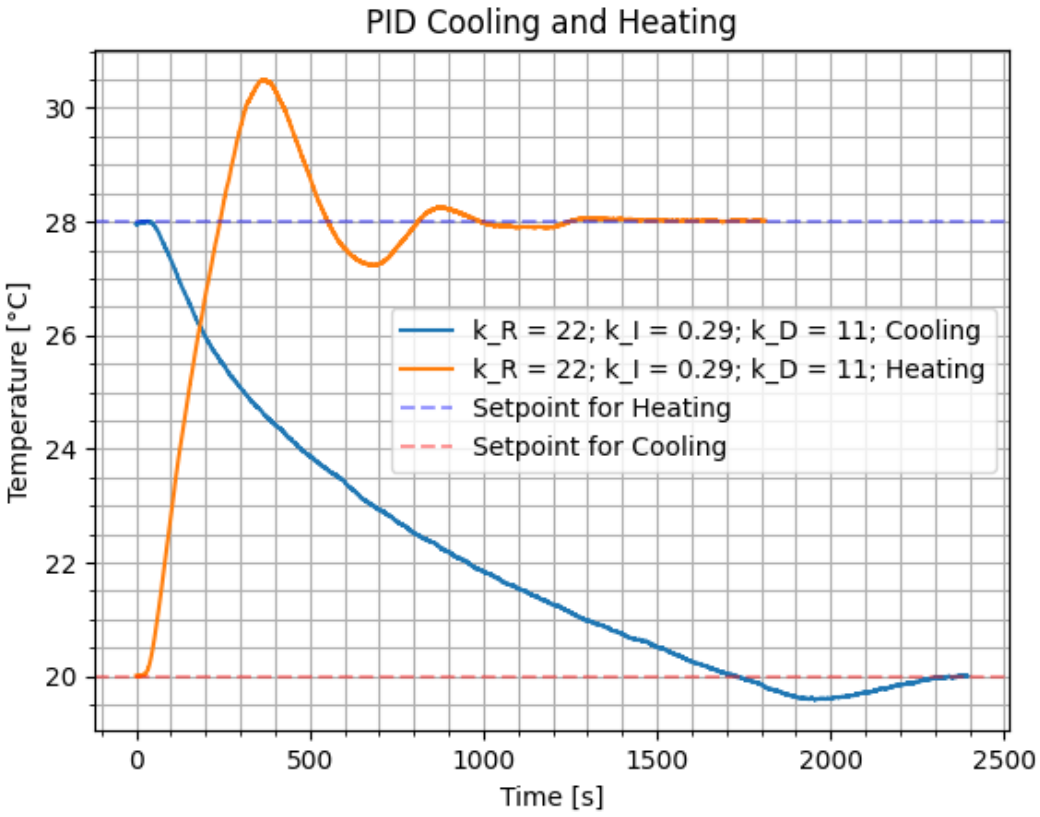

Figure 3.15: Test of final PID controller tuning for heating and cooling

4. Measurements and Tests

4.1 Preparations

To prepare for testing, the measurement system had to be equipped with various sensors for detailed monitoring of conditions. As thermal stability is a crucial aspect during the measurements and tests, a temperature monitoring system was set up first. The system consists of a Raspberry Pi 4B that is equipped with five DS18B20 digital temperature sensors. The DS18B20 has an accuracy of $\pm 0.5\,^{\circ}\mathrm{C}$, which is sufficient, because the absolute temperature value is of secondary importance compared to the relative temperature variations. These are registered reliably, as the DS18B20 has a resolution of $0.0625\,^{\circ}\mathrm{C}$. The sensors are connected to the microcomputer's general purpose input and output (GPIO) pins, allowing for a straightforward readout of digital temperature values. Communication via a 1-wire bus simplifies the integration of multiple sensors. In total, five sensors were installed to monitor the thermal behavior inside the Zarges box in multiple test scenarios. The temperature sensors are placed in five different locations, illustrated in Figure 4.1:

1. Left side inside the box: This sensor monitors the side closest to the TEM, where the lowest temperatures are anticipated. Furthermore, this sensor could help visualize the control action.

2. Right side inside the box: The sensor is placed on the opposite side of sensor 1 because an inhomogeneous temperature distribution is expected.

3. Center of the lower level: The power supplies of all devices are located on this level. The sensor is intended to monitor if there are temperature fluctuations as a result of the dissipated heat. Since the heat dissipation is expected to be constant, only small effects on the temperature are anticipated.

4. Upper level, next to the spectrometer: This sensor is located next to the spectrometer in the same position as the input thermometer of the temperature control. This is the position where temperature stability must be ensured. Effects on the spectral shift of the spectrometer are anticipated to be the result of the temperature variations measured by this sensor (see Section 2.3.3).

5. Outside of the box: This sensor measures ambient temperature. The temperature control is intended to compensate for fluctuations in this value.

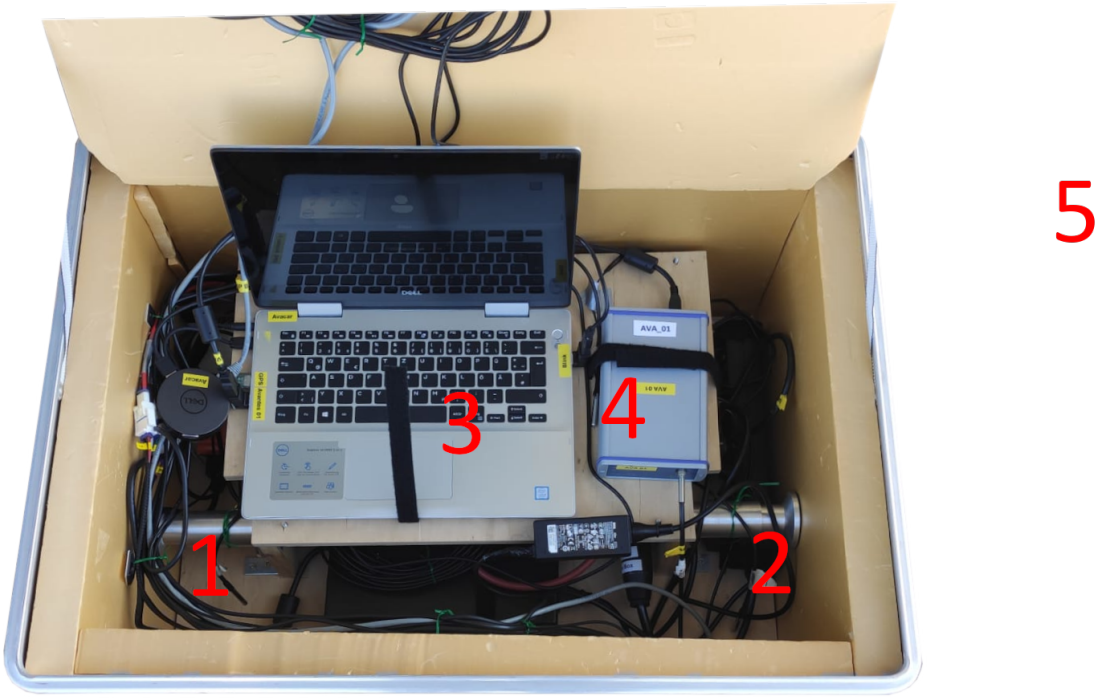

Figure 4.1: Temperature sensor positions: 1. left side, 2. right side, 3. lower level (hidden from view), 4. upper level, 5. outside

The temperature data are logged at predefined intervals and reported daily via email using a Python script.

In addition to temperature monitoring, a humidity sensor was installed for more detailed characterization of the box's interior conditions. Furthermore, the controller circuit board temperature and the spectrometer's temperature are tracked as supplementary parameters using already integrated temperature sensors.

4.2 Measurement Scenarios

4.2.1 Laboratory

In the first scenario, the measurement system was set up in the laboratory, which was not air conditioned during the testing period. The objective of this test was to expose the temperature-controlled system to moderate temperature fluctuations to assess the performance of the temperature control. At the same time, DOAS measurements were carried out to obtain data on the resulting spectral shift.

The telescope for spectroscopic measurements was pointed out of the window, and measurements were conducted at a single elevation angle. The temperature setpoint was 19 °C.

4.2.2 Rooftop

The second scenario was a complete MAX-DOAS setup on the roof of the University of Bremen's NW1 building. The measurements were conducted to obtain data for a comparison with the operational Institut für Umweltphysik Bremen (IUPB) MAX-DOAS device, which is used as a reference instrument since it routinely provides quality-assured data. Larger ambient temperature fluctuations were expected due to the system's direct exposure to weather. This scenario placed greater demands on the temperature control system. The MAX-DOAS measurements were carried out in multiple viewing azimuth angles with elevation angles in a range of $-1°$ to $30°$ with a reference spectrum measured at $90°$. The temperature setpoint was 22 °C. The rooftop setup is shown in Figure 4.2.

Figure 4.2: Measurement setup on the NW1 rooftop

4.2.3 Core Repository

The international core repository at the MARUM Center for Marine Environmental Sciences is operated at the University of Bremen and contains drill cores from the Atlantic Ocean, Mediterranean, Black and Baltic Seas and Arctic Ocean which were collected in multiple deep sea and ocean drilling programs [27]. The cores are kept in a refrigerated storage area, that provides suitable conditions to test the measurement system's temperature stability in a heating or near-heating scenario. The box

was placed in the storage area where the expected ambient temperature was around 4 °C. Due to issues with the refrigeration, which were fixed shortly before the test, the ambient temperature was higher than the expected value and slowly decreased during the test. The temperature setpoint was 22 °C. The spectrometer was operated without a telescope, so no meaningful measurement data were acquired. Instead, it was run to simulate the computational load and associated heat dissipation that would occur during a real deployment. The MARUM setup is shown in Figure 4.3.

Figure 4.3: Measurement setup in the MARUM core repository

4.3 Results

4.3.1 Temperature Control Performance Testing

The performance of the measurement system was tested under laboratory, rooftop and MARUM conditions to assess its ability to stabilize its temperature in cooling, heating, and dynamically changing scenarios.

Laboratory

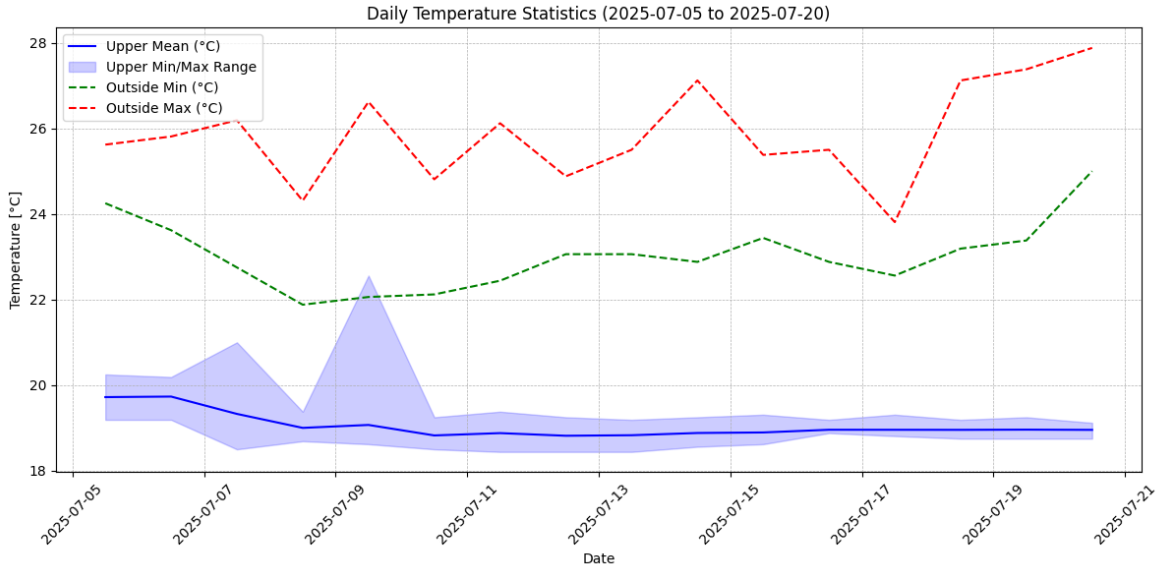

Figure 4.4: Temperature statistics for measurements under laboratory conditions. Temperatures were obtained by upper level and ambient temperature sensors.

Figure 4.4 shows the daily control temperature average for the laboratory testing period together with its respective daily minima and maxima and the ambient temperature minima and maxima. The high deviations between control temperature maxima and the average on July 7 and 9 (see Figure 4.6a) are caused by maintenance activities, where the box was opened. It can be seen that during undisturbed operation, from July 11 onward, only small deviations in the order of $\pm 0.6\,\mathrm{K}$ from the setpoint of $19\,^{\circ}\mathrm{C}$ occurred. The ambient temperature ranged from $22\,^{\circ}\mathrm{C}$ to $28\,^{\circ}\mathrm{C}$. Within this range, no correlation between the upper level temperature and the ambient temperature is apparent.

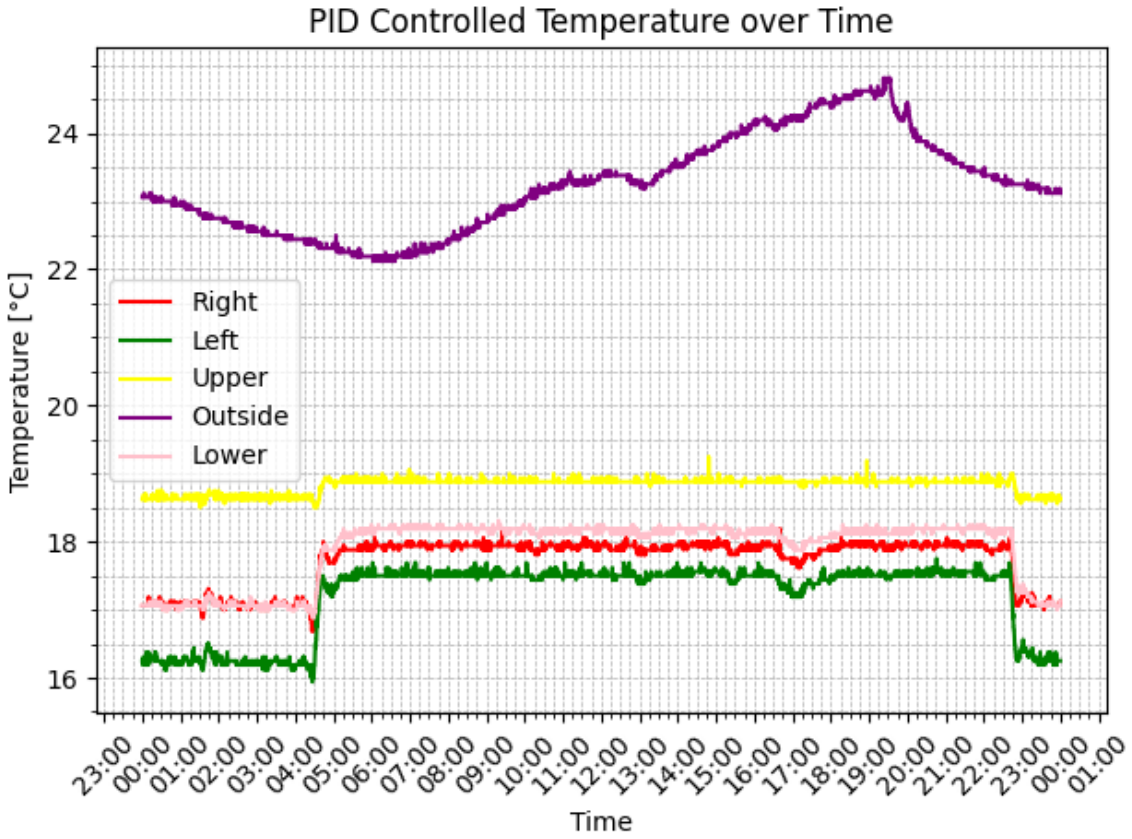

Figure 4.5: Temperatures on July 10 2025 in the laboratory setup

Figure 4.5 depicts the temperature data in more detail over one day, July 10. The ambient temperature, depicted by the purple curve, shows only moderate deviations. The temperatures within the box exhibit excellent stability. In particular, the crucial temperature value next to the spectrometer, denoted as "Upper" since the temperature sensor was placed on the upper level of the rack, fluctuates only at 4:30 and at 22:30. These fluctuations are due to the beginning and end of the spectrometer measurements, resulting in an increased computational load, which leads to a higher heat dissipation by the computer. Changes in ambient temperature did not noticeably influence the temperatures inside the box, indicating that especially slow changes in disturbances are mitigated without problems.

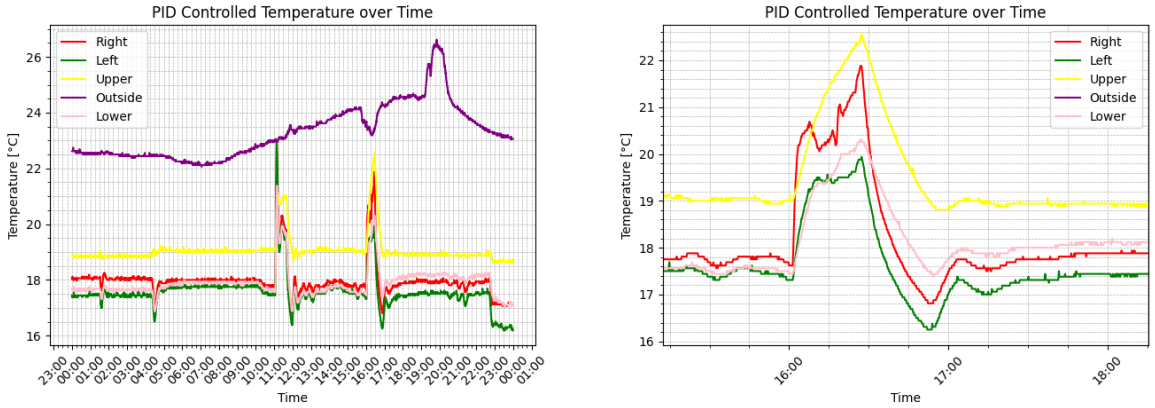

(a) Temperature curves including a disturbance by opening the box

(b) Detailed depiction of the disturbance

Figure 4.6: Temperatures on July 9 2025 in the laboratory setup

Figure 4.6a shows the temperatures during laboratory testing on July 9. There are two peaks in the four interior temperatures which were caused by opening the box for maintenance. Figure 4.6b, which depicts the disturbance in detail, indicates that the fast disturbance is mitigated in approximately one hour. The upper level temperature increased by 3.5 K before it started to decrease. The temperature overshot by 0.2 K and stabilized without oscillations, indicating stable control performance under laboratory conditions.

Rooftop

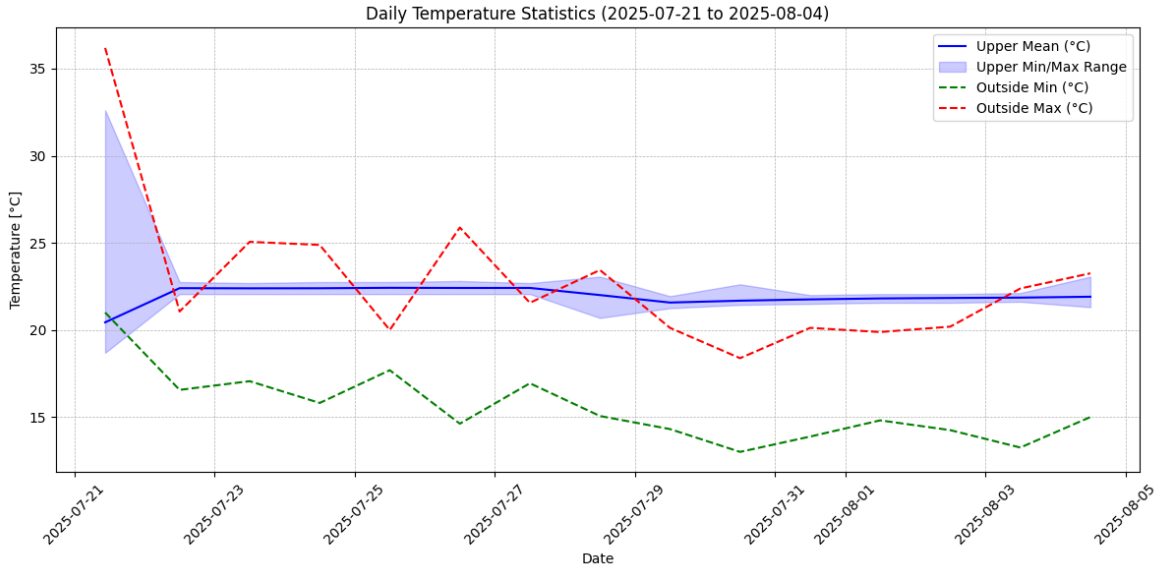

Figure 4.7: Temperature statistics for measurements on the rooftop of the NW1 building

From July 21 to August 4, the measurement system operated on the rooftop of the NW1 building. As shown in Figure 4.7 after the setup on July 21, the temperature remains very stable regardless of whether the control temperature was higher or lower than the ambient temperature.

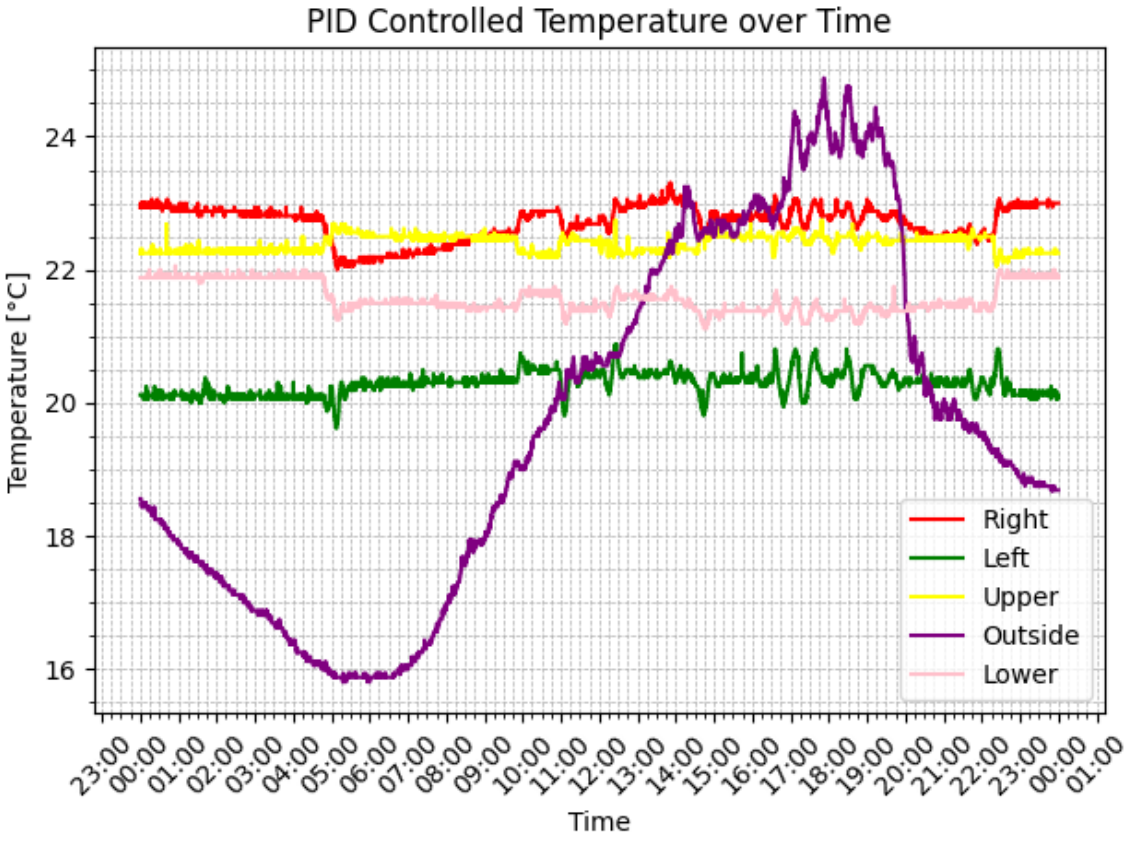

Figure 4.8: Temperatures on July 24 2025 in the rooftop setup

Figure 4.8 illustrates that the controlled temperature on the rooftop is less stable than under laboratory conditions (see Figure 4.5), although it is still reasonably stable within approximately $\pm 0.4\,\mathrm{K}$. The reduced stability is likely due to stronger variations in ambient temperature on the rooftop compared to the laboratory, environmental disturbances such as wind and solar irradiation, and additional thermal load caused by the operation of the pan-tilt head, which was inactive during controller tuning. Since the controller was tuned under laboratory conditions, its parameters may not fully account for these rooftop disturbances.

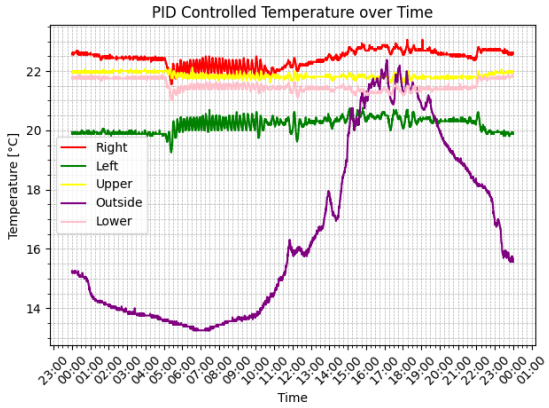

(a) Temperature oscillations on August 3 2025

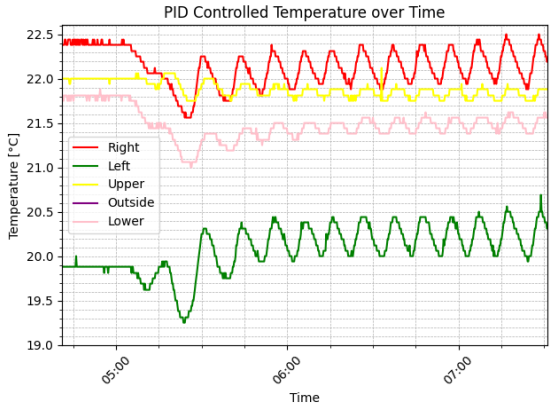

(b) Detailed depiction of temperature oscillations on August 3 2025

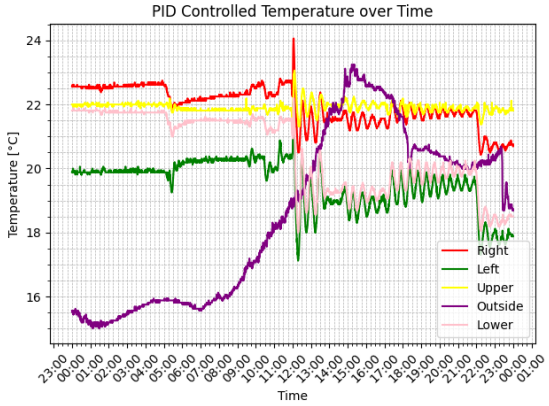

(c) Temperature oscillations on August 4 2025

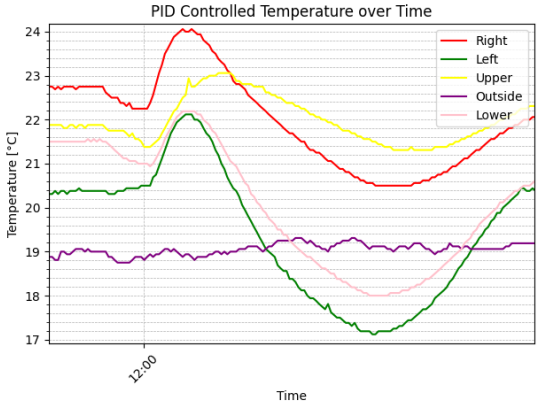

(d) Detailed depiction of temperature oscillations on August 4 2025

Figure 4.9: Oscillating behavior of temperature during two measurement days on the rooftop of the NW1 building

Figure 4.9 shows two days of measurements on August 3 and 4. It suggests that the system is prone to oscillations that appear to be caused by an overly strong controller response to fast-varying disturbances under certain conditions. In Section 3.6, Figure 3.15 shows that for the tuning compromise between heating and cooling the temperature tends to oscillate in heating scenarios in particular. Under laboratory conditions, the control temperature settles within approximately two hours. It is likely that disturbances, which were not accounted for during tuning, lead to insufficient damping of the oscillations. Further possible reasons include mis-tuning, especially of the derivative action that might amplify and react to measurement noise. Another possible reason is variations in the heat load from the pan-tilt head power supply. Figure 4.9d depicts what can be interpreted as the control response to a disturbance. The control temperature, represented by the yellow curve, decreases by 0.4 K at 12:00. After the decrease, the temperature nearest to the TEM, represented by the green

curve, increases immediately by approximately 1.6 K. This suggests that the overly strong control response results in oscillations.

MARUM

During the test of the measurement system in the MARUM Core Repository between August 6 and August 15, no internet connection was available. Hence, the Raspberry Pi experienced a time shift of approximately 19 hours that was corrected by concatenating all temperature files, applying the respective time shift, and re-splitting the data into daily files. Since the exact temporal shift could not be reconstructed, there might still be a minor absolute time difference. However, the temperature values remain unaffected by this correction.

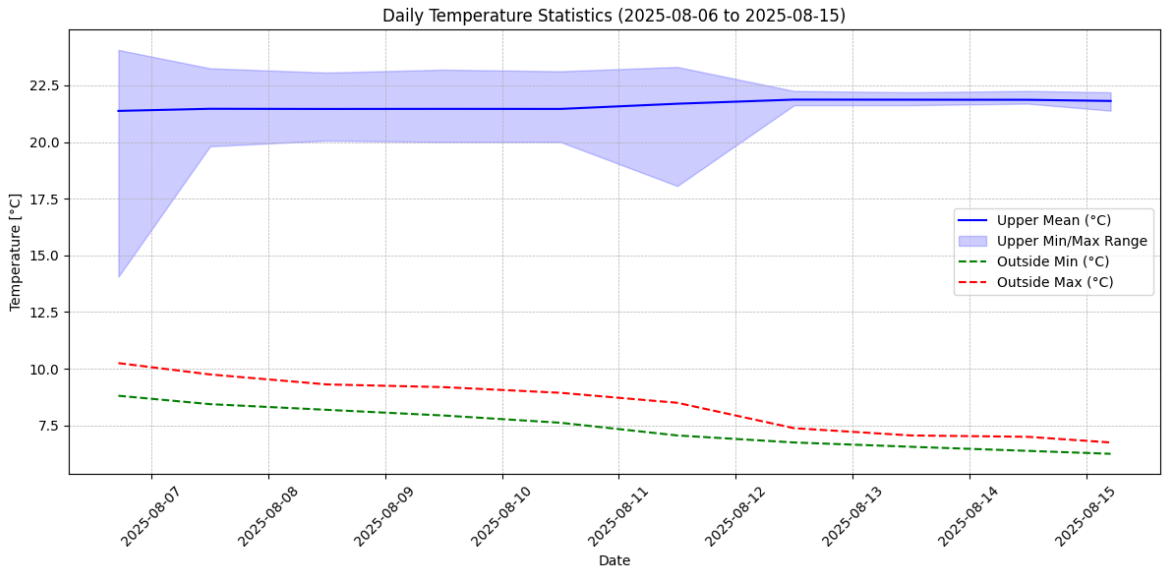

Figure 4.10: Temperature statistics for measurements in the MARUM Core Repository

Figure 4.10 shows that there were higher temperature variations in the order of ±2 K around the mean value in the period between August 6 and August 12. The high negative deviation on August 6 is caused by the box being open during setup. During the measurement period, the ambient temperature in the core repository was decreased from approximately 10 °C to 6 °C. The temperature change is very slow, which means that it is not a disturbance that should affect the control. Instead, the temperature control is unstable as shown in Figure 4.11.

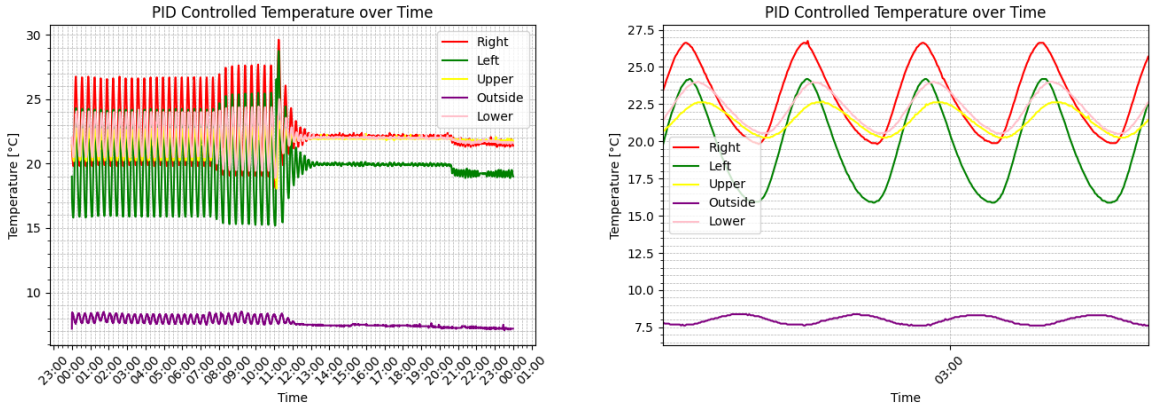

(a) Oscillating temperatures during the MARUM Core Repository test

(b) Detailed depiction of the oscillating temperatures

Figure 4.11: Temperatures on August 11 2025

Figure 4.11b illustrates the oscillating behavior of the temperatures. The control temperature oscillates around the set point temperature of 22 °C, ranging from 20 °C to 22.5 °C. It becomes obvious that the controller is tuned overly aggressive for a pure heating or near-heating scenario. The ambient temperature also oscillates, which is likely caused by the air flow from the outer TEM fan. That is indicated by the rise of the ambient temperature when the TEM starts to cool, represented by the decrease of the green curve, and vice versa. To stabilize the temperatures, the control parameters were reduced to $K_R = 14$, $K_I = 0.2$ and $K_D = 4$. After re-tuning at 11:30, the temperatures settled as shown in Figure 4.11a.

4.3.2 Humidity

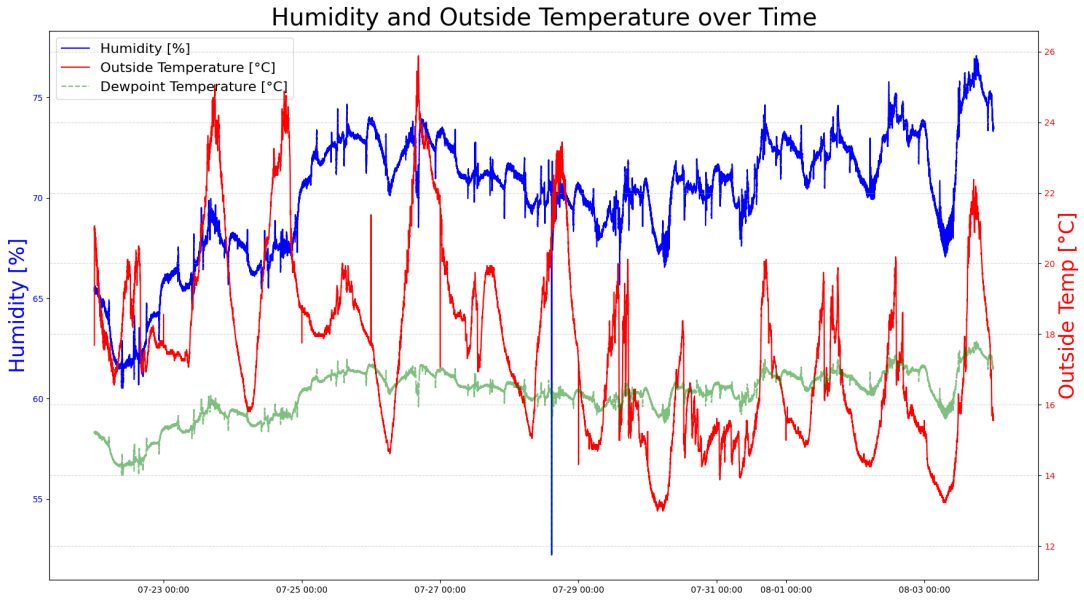

Figure 4.12: Relative humidity, ambient temperature and dewpoint temperature for measurements between July 22 and August 4

Figure 4.12 shows the relative humidity inside the box, the ambient temperature, and the dewpoint temperature measured between July 22 and August 4 on the NW1 rooftop. During this period, the relative humidity inside the box ranged from approximately 63 % to 78 %.

The measurement box is maintained at a nearly constant temperature of 22 °C, and moisture enters only slowly from the outside environment. Daily fluctuations in the outside temperature have little immediate effect on the relative humidity inside. However, when the ambient temperature drops below the dewpoint, condensation occurs on the aluminum walls, which are assumed to have a temperature similar to the ambient air. This removes water from the air in the box, leading to local minima in relative humidity during cooler periods, as observed in the plot.

To assess under which conditions condensation is expected to occur, the dewpoint temperature can be calculated using the Magnus formula:

$$T_d = \frac{b \cdot \alpha(T,\varphi)}{a - \alpha(T,\varphi)}, \quad \alpha(T,\varphi) = \ln\left(\frac{\varphi}{100}\right) + \frac{aT}{b+T}, \tag{4.1}$$

where T denotes the air temperature, φ is the relative humidity in % and the constants are $a = 17.5$ and $b = 241.2\,°\mathrm{C}$. Figure 4.13 illustrates the dependence of the dewpoint on air temperature and

relative humidity.

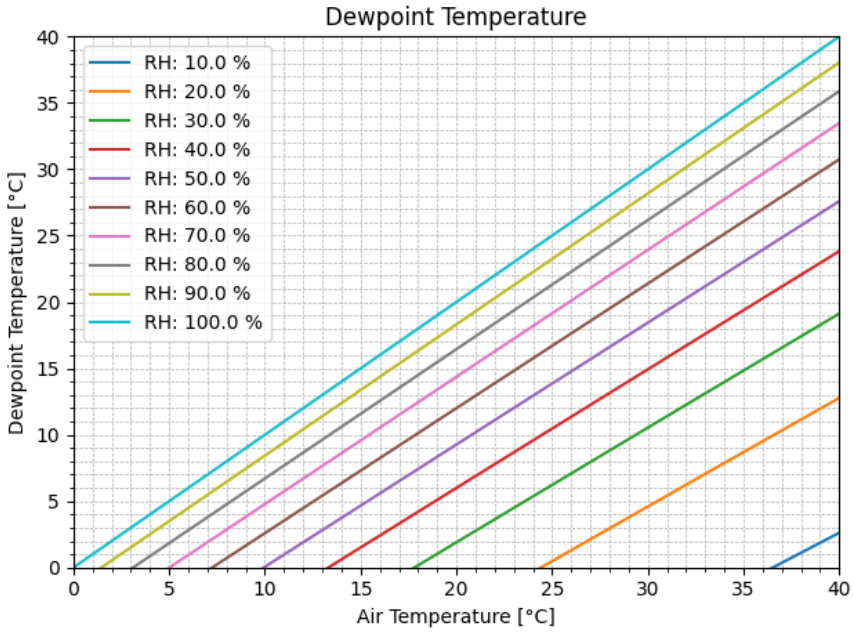

Figure 4.13: Dewpoint temperature in dependence on air temperature and relative humidity

The plot indicates that condensation will occur on the inside of the aluminum walls when the system is operated in cold environments, when even low relative humidity can be sufficient, or on the cold side of the TEM in hot and very humid environments, where the dewpoint temperature is close to the air temperature.

4.3.3 Comparison with IUPB MAX-DOAS

To assess the data quality of the Zarges DOAS measurement system, the results were compared to the MAX-DOAS instrument of the Institut für Umweltphysik Bremen (IUPB). The IUPB instrument is an Acton500 Czerny-Turner spectrometer with a spectral range of 406 nm to 579 nm. It incorporates a Princeton NTE/CCD-1340/100-EMB CCD, which is cooled to −30 °C. The Styrodur-enclosed IUPB MAX-DOAS instrument is located in an air-conditioned laboratory and is connected via an optical fiber to a telescope, which is equipped with a pan-tilt head. To maximize the number of directly comparable data points both instruments were restricted to two viewing azimuth angles, 270° and 295°, and were operated so that they observe the same viewing direction close in time.

Horizon Scan

Both instruments perform a horizon scan daily at 13:00. During these scans, the instruments record the averaged signal intensity at elevations ranging from −2.5° to 2.5° with a step size of 0.1°. The

obtained data, depicted in Figure 4.14, can be used to determine at which viewing elevation the horizon is located and, hence, whether the instruments' viewing elevations are aligned. Additionally, the field of view of each instrument can be estimated from the data.

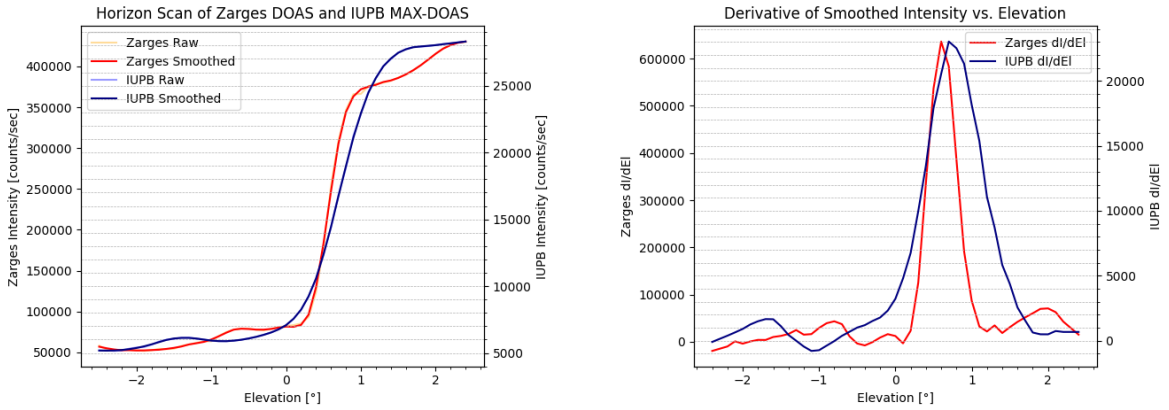

(a) Raw and smoothed horizon scans

(b) Derivatives of the intensities with respect to elevation angle

Figure 4.14: Comparison of the horizon scans obtained with Zarges DOAS and IUPB MAX-DOAS

Figure 4.14a shows the measured intensity depending on the elevation angle, and Figure 4.14b shows its derivatives with respect to the elevation angle. The location of the peak of each curve indicates where the horizon appears for the respective instrument. The horizon is observed at 0.6° by the Zarges DOAS, and at 0.7° by the IUPB MAX-DOAS instrument, which means that the latter is oriented 0.1° lower. The instruments' field of view is determined from the full width at half maximum (FWHM) of the derivative curves, yielding a field of view of approximately 0.5° for the Zarges DOAS instrument and 0.8° for the IUPB MAX-DOAS instrument. The difference in field of view is expected due to instrument design. The Avantes spectrometer employed in the Zarges DOAS uses a narrower entrance slit. Hence, fewer optical fibers are required for coupling, reducing the instrument's field of view. These results confirm that both instruments are properly aligned, providing a solid basis for subsequent comparison of their measurements.

Spectral Shift

An important parameter for assessing the measurement quality is the spectral shift caused by temperature fluctuations in the spectrometer and the detector (see Section 2.3.3, Equation 2.22). Thermal variations can shift the position of a measured atmospheric spectrum with respect to the reference spectrum, here taken around noon, and can thereby introduce significant errors in the spectral fit [2].

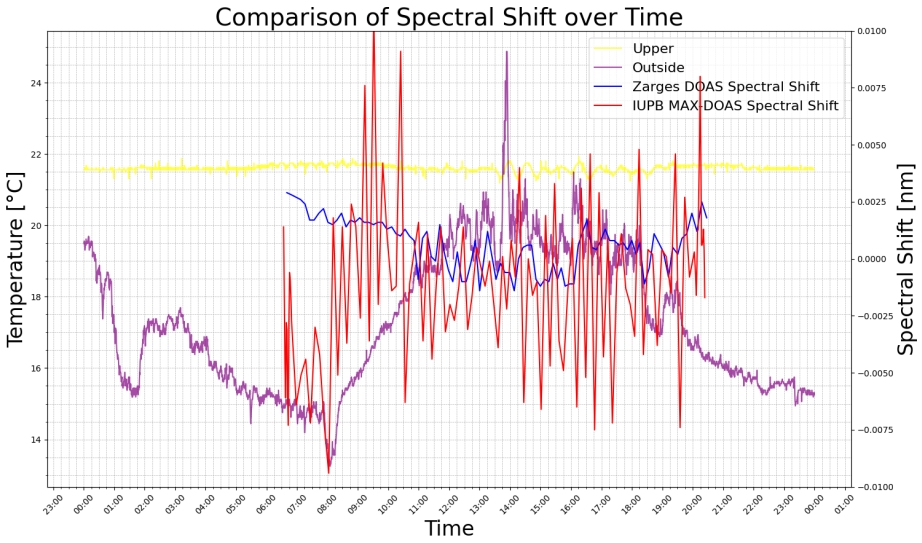

Figure 4.15: Spectral shift of Zarges DOAS and IUPB MAX-DOAS instruments on August 21 2025

Figure 4.15 shows the spectral shift of the Zarges DOAS and IUPB MAX-DOAS instruments during zenith sky measurements, as well as the outside temperature and PID-controlled temperature in the Zarges DOAS measurement system close to the spectrometer. In both cases, there is no apparent dependency between the shift and the outside temperature, which indicates sufficient thermal stability in both setups. The spectral shift in the IUPB setup ranges approximately from $-0.01\,\text{nm}$ to $0.01\,\text{nm}$ while it only ranges approximately between $-0.001\,\text{nm}$ and $0.003\,\text{nm}$, i.e. about one order of magnitude smaller, in the Zarges measurement system, although the Zarges DOAS is placed outside and the MAX-DOAS is placed in the laboratory. These results demonstrate that the Zarges DOAS system provides highly stable measurement conditions within the tested temperature range.

Slant Column Densities

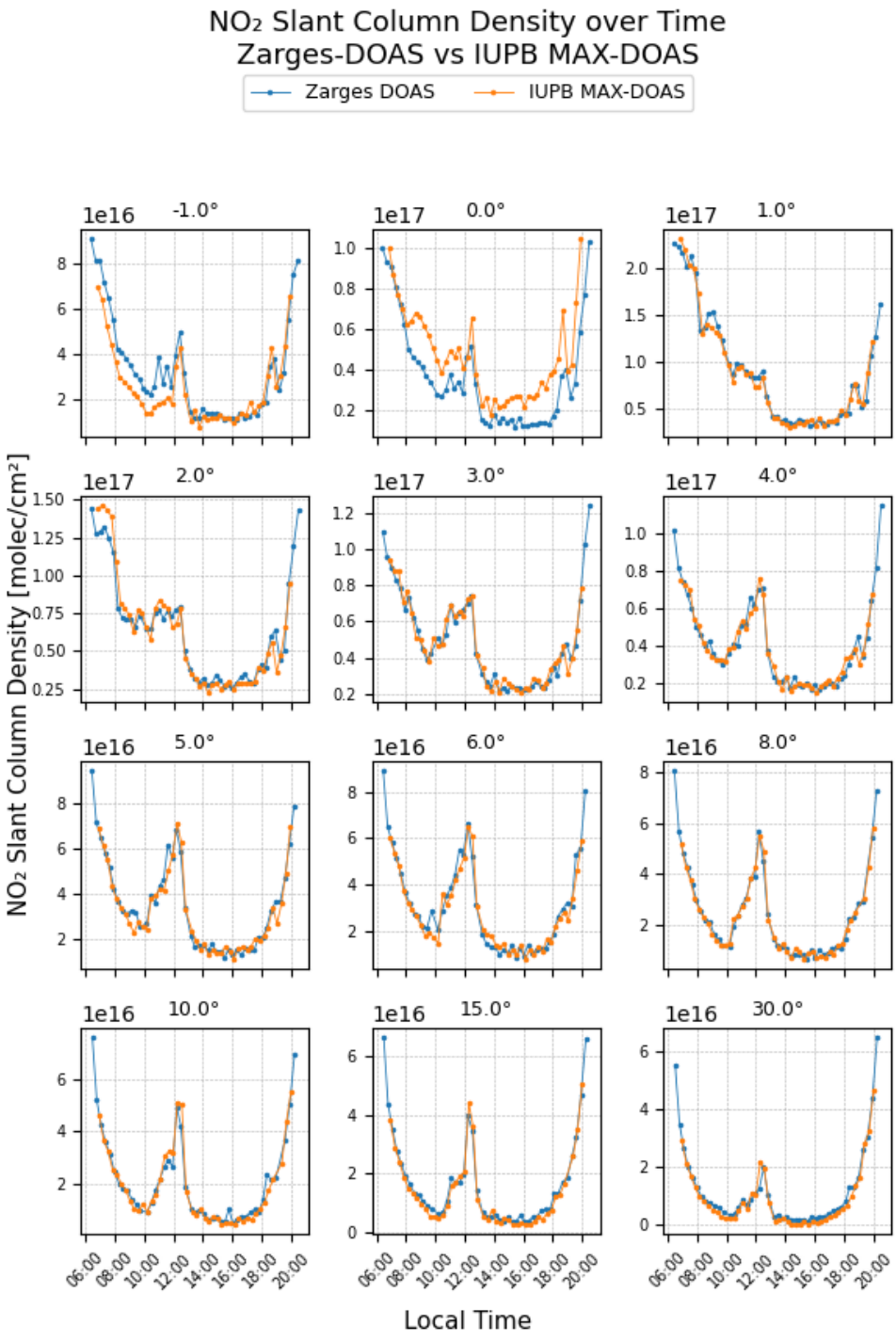

Figure 4.16: Comparison of NO_2 slant column density time series obtained by Zarges DOAS and IUPB MAX-DOAS on August 21 2025

A further step of the assessment of the Zarges DOAS measurement system's performance is the comparison of the SCD time series obtained with both instruments. The data from which the slant column densities were retrieved were acquired exclusively in the 270° azimuth angle viewing direction. The measurements were taken at 12 viewing elevations ranging from −1° to 30°. Figure 4.16 shows the results of the DOAS fit. The y-axis limits are specifically chosen for each elevation angle in order to depict the details in each elevation angle.

The plots show that the retrieved NO_2 slant column densities are particularly large during dusk and dawn. This is due to the high solar zenith angle: the low sun position leads to a longer light path, which changes the respective air mass factor and results in larger NO_2 SCDs. Also, at the lower elevations of 0° to 4° the SCDs are one order of magnitude larger than at other elevations, which can also be explained by prolonged light paths for those viewing geometries (see Section 2.3.3, Figure 2.9).

There is a peak in the SCDs that is particularly distinct in elevations 3° to 30°. As both instruments show the exact same peak neither a hardware fault nor a DOAS fitting error appears plausible. It is likely that the peak is caused by an NO_2 emission event near the measurement site, a plume from industrial facilities that has been transported to the line of sight or simply the influence of light path enhancements in clouds.

At an elevation of −1° the Zarges DOAS instrument slightly overestimates NO_2 SCDs, whereas it tends to underestimate SCDs at 0°. The discrepancy between the instruments at these low elevation angles is likely caused by their difference in field of view (see Section 4.3.3). Differences in apparent horizon and FOV cause the instruments to sample slightly different fractions of near-ground reflected light, contributing to the observed discrepancies at low elevations. At elevations where those ground-reflection effects do not significantly affect the signal intensity, the Zarges DOAS measurement system and the IUPB MAX-DOAS instrument exhibit very good agreement. Minor differences in SCD are observed mainly when measurements were not strictly simultaneous, likely reflecting real temporal variability of NO_2 rather than instrumental bias.

To quantify the agreement between the two instruments an orthogonal distance regression (ODR) was performed, complemented by the calculation of the Pearson correlation coefficient. ODR has the advantage over a linear regression that the independent variable, here the SCD retrieved from the IUPB MAX-DOAS instrument, is not assumed to be error-free. However, the results of a linear regression were used as an initial guess of the slope and intercept for the ODR. The regression yields the slope and the intercept. The ideal value of the slope would be 1, indicating perfect agreement, and the ideal value of the intercept is 0, indicating the absence of bias. To ensure comparability, the data of the two instruments were filtered to have a time difference smaller than five minutes while observing

the same elevation.

The Pearson correlation coefficient r quantifies the strength and direction of a linear relationship, with $r = 1$ indicating a perfect positive correlation and $r = -1$ a perfect negative correlation. The associated p-value assesses the statistical significance, with low values suggesting that the observed correlation is unlikely to occur by chance. The Pearson coefficient and the ODR results are complementary. While r describes the correlation strength, ODR provides a test of systematic agreement through the fitted slope and intercept.

Table 4.1: Regression results of Zarges-DOAS vs IUPB MAX-DOAS NO_2 slant column densities at different elevation angles

Elevation (°)	Slope	Intercept	r	p
-1	0.903	5.48×10^{15}	0.848	1.65×10^{-7}
0	0.622	1.79×10^{15}	0.894	8.95×10^{-9}
1	0.961	3.11×10^{15}	0.951	3.89×10^{-12}
2	0.938	3.76×10^{15}	0.97	1.99×10^{-14}
3	0.945	1.69×10^{15}	0.982	9.74×10^{-17}
4	0.977	4.98×10^{14}	0.978	1.06×10^{-15}
5	0.982	3.57×10^{14}	0.978	1.82×10^{-16}
6	1.05	-1.87×10^{15}	0.975	7.29×10^{-16}
8	0.967	6.87×10^{13}	0.994	7.19×10^{-22}
10	0.854	2.21×10^{15}	0.991	3.67×10^{-19}
15	0.889	1.8×10^{15}	0.994	6.26×10^{-21}
30	0.877	1.35×10^{15}	0.979	1.45×10^{-14}

Table 4.1 shows the results of the ODR and the calculation of the Pearson correlation coefficient. The values indicate that the Zarges DOAS measurement system and the IUPB MAX-DOAS instrument show very good agreement at elevations between 1° and 8°. For these elevations, the resulting slope deviates slightly from unity, indicating that both instruments provide nearly identical retrieval. At elevations $-1°$ and 0° the slope deviates more strongly from unity (0.62 at 0°). Figure 4.17 shows this particularly at 0°. At $-1°$ the bias, represented by the intercept, is slightly higher, which leads to an overestimation at lower SCDs and, resulting from the lower slope, an underestimation at higher SCDs. The reasons for this disagreement at low elevations are explained above.

At elevations between 10° and 30°, the slopes decrease and range between 0.854 and 0.889. Although these values still indicate reasonably good agreement, the deviation between the two instruments is higher than at elevations 1° to 8°. Possible reasons are differences in instrumental setups like FOV and sensitivity, which become relatively more influential at higher elevations than at lower ones. Changes in cloud coverage may also influence the result. Another explanation is the low number of measurement points. The reduced number of data points means that single outliers have a stronger influence on the regression parameters.

The Pearson coefficients for all elevations from 1° to 30° are larger than 0.95, further confirming the

notion of a strong positive correlation. At the low elevations, the Pearson coefficients are slightly lower, indicating a less consistent correlation. The p-values are $\ll 0.05$, confirming that the correlations are highly statistically significant.

Overall, the Zarges DOAS shows very good agreement with the operational IUPB MAX-DOAS, especially between 1° and 8°. Deviations at very low and very high elevation angles are consistent with expected geometric and sensitivity limitations, rather than indicating fundamental problems with the instrument.

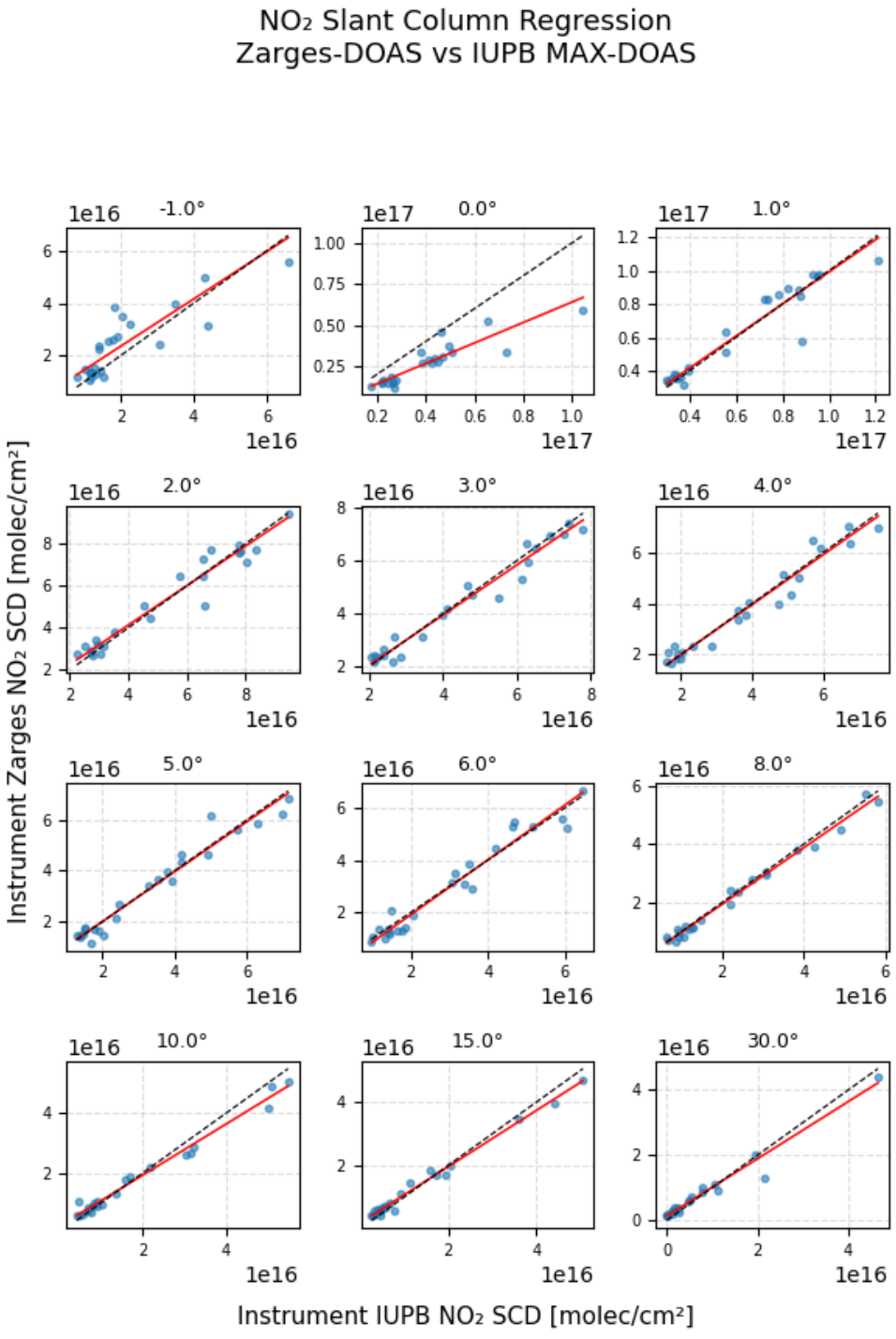

Figure 4.17: Orthogonal distance regression of NO_2 SCDs retrieved by Zarges DOAS against IUPB MAX-DOAS on August 21 2025. The respective regression parameters and statistical measures are provided in Table 4.1.

5. Conclusion and Outlook

This thesis presents the design, assembly, and testing of a thermally stabilized measurement system for differential optical absorption spectroscopy that is suitable for outdoor applications. As a first step, the theoretical background, including scientific information on the composition of Earth's atmosphere and radiative transfer, as well as technical information on spectroscopy in general and DOAS in particular, is elaborated. Furthermore, the elements of the temperature stabilization, the thermoelectric module, and the PID control itself are explained.

The theoretical part is followed by an engineering section. In this subsequent chapter, the setup of the Zarges DOAS measurement system is described. According to predefined design specifications and the calculation of the required thermoelectric module's cooling capabilities, a design was developed, and the measurement system was assembled. The construction of the measurement system was finished by tuning a PID controller to ensure stable temperature control for both heating and cooling scenarios.

The performance of the measurement system was evaluated under laboratory, rooftop and refrigerated storage conditions. The results demonstrate that the thermal control works reliably under diverse conditions, although oscillations occurred in some scenarios. The control instability was mitigated by controller re-tuning. Under rooftop conditions a very low spectral shift, ranging from approximately $-0.001\,\mathrm{n}$ to $0.003\,\mathrm{n}$, is achieved. Finally, the system was validated against the operational IUPB MAX-DOAS instrument. The comparison showed good agreement, confirming that the Zarges DOAS measurement system provides high-quality data for DOAS retrieval.

Although a functioning measurement system was developed in the course of this thesis, some challenges will need to be addressed. The temperature control requires further testing and refinement to ensure robustness and stability under a wider range of thermal conditions and to understand its boundaries. Humidity levels, which were found to be high, should be decreased more efficiently, and the whole measurement system will need to be sealed more thoroughly, especially if a deployment under harsh environmental conditions is planned.

Future work should include extended field deployments to fully assess performance under harsh and

varying conditions. The good agreement with the IUPB MAX-DOAS instrument implies that the Zarges DOAS system has the potential to become a cost-effective, easy-to-use, and portable instrument for DOAS measurements, which is suitable for research campaigns.

Bibliography

[1] World Health Organization. "Ambient (outdoor) air pollution." (Oct. 24, 2024), [Online]. Available: https://www.who.int/news-room/fact-sheets/detail/ambient-(outdoor)-air-quality-and-health (last visited on 08/30/2025).

[2] U. Platt and J. Stutz, *Differential optical absorption spectroscopy, Principles and applications* (Physics of Earth and Space Environments). Berlin, [Germany] ; Springer, 2008, 1608 pp., Includes bibliographical references at the end of each chapters and index. Description based on print version record. "With 272 Figures and 55 Tables.".

[3] J. M. Wallace and P. V. Hobbs, *Atmospheric science, An introductory survey* (International geophysics series 92), 2. ed., [2. repr.] Amsterdam: Academic Press, 2008, 483 pp.

[4] NASA's Jet Propulsion Laboratory. "The Atmosphere: Getting a Handle on Carbon Dioxide." A. Buis, Ed. (Oct. 22, 2024), [Online]. Available: https://science.nasa.gov/earth/climate-change/greenhouse-gases/the-atmosphere-getting-a-handle-on-carbon-dioxide/#hds-sidebar-nav-2 (last visited on 09/01/2025).

[5] M. Thürkow, S. Banzhaf, T. Butler, J. Pültz, and M. Schaap, "Source attribution of nitrogen oxides across Germany: Comparing the labelling approach and brute force technique with LOTOS-EUROS," *Atmospheric Environment*, vol. 292, p. 119 412, Jan. 2023. DOI: 10.1016/j.atmosenv.2022.119412.

[6] Deutscher Wetterdienst. "Nitrogen oxides (NO, NO2, NOx, NOy)." (n.d.), [Online]. Available: https://www.dwd.de/EN/research/observing_atmosphere/composition_atmosphere/trace_gases/cont_nav/nox_node.html (last visited on 08/05/2025).

[7] L. Wang and J. Yu, "Principles of photocatalysis," in *S-scheme Heterojunction Photocatalysts - Fundamentals and Applications*. Elsevier, 2023, pp. 1–52. DOI: 10.1016/b978-0-443-18786-5.00002-0.

[8] M. Paulescu and V. Badescu, "Spectral nature of solar radiation," in *Spectral Characteristics of Solar Radiation*. Elsevier, 2025, pp. 3–32. DOI: 10.1016/b978-0-443-23839-0.00001-8.

[9] U. J. Krull and M. Thompson, "Analytical Chemistry," in *Encyclopedia of Physical Science and Technology*. Elsevier, 2003, pp. 543–579. DOI: 10.1016/b0-12-227410-5/00025-9.

[10] Thorlabs. "Diffraction Gratings Tutorial." (2025), [Online]. Available: https://www.thorlabs.com/newgrouppage9.cfm?objectgroup_id=9026 (last visited on 07/20/2025).

[11] N. Alfaraj, "A review of charge-coupled device image sensors," en, unpublished, 2017. DOI: 10.13140/RG.2.2.10971.77608.

[12] Le Mans Université. "Basic principles of image sensors." P. Slangen, Ed. (2023), [Online]. Available: https://perso.univ-lemans.fr/~fvaret/opi/cours_maj/OPI_ang_M05_C06_web_gen_auroraW/co/Contenu_04.html#:~:text=The%20technology%20on%20which%20CCD,far%20infrared%20to%20X-rays. (last visited on 07/22/2025).

[13] Teledyne Imaging. "How a Charge Coupled Device (CCD) Image Sensor Works, 50 years of the ccd." (2020), [Online]. Available: https://www.teledyneimaging.com/media/1300/2020-01-22_e2v_how-a-charge-coupled-device-works_web.pdf (last visited on 07/22/2025).

[14] L. Shen, X. Feng, Y. Zhang, M. Shi, D. Zhu, and Z. Wang, "Stroboscope Based Synchronization of Full Frame CCD Sensors," *Sensors*, vol. 17, no. 4, p. 799, Apr. 2017. DOI: 10.3390/s17040799.

[15] J. P. Burrows, U. Platt, and P. Borrell, *The Remote Sensing of Tropospheric Composition from Space* (SpringerLink), A. Richter and T. Wagner, Eds. Berlin, Heidelberg: Springer-Verlag Berlin Heidelberg, 2011, ch. Chapter 2 Solar Backscattered Radiation: UV, Visible and Near IR – Trace Gases, 67 to 122, 536130 pp., Includes bibliographical references and index.

[16] G. Pinardi, M. Van Roozendael, F. Hendrick, *et al.*, "Validation of tropospheric NO2 column measurements of GOME-2A and OMI using MAX-DOAS and direct sun network observations," *Atmospheric Measurement Techniques*, vol. 13, no. 11, pp. 6141–6174, Nov. 2020. DOI: 10.5194/amt-13-6141-2020.

[17] University of Bremen IUP DOAS. "The MAXDOAS instrument and measurements." (2025), [Online]. Available: https://www.iup.uni-bremen.de/doas/maxdoas_instrument.htm (last visited on 07/29/2025).

[18] X. Zhu, Y. Yu, and F. Li, "A review on thermoelectric energy harvesting from asphalt pavement: Configuration, performance and future," *Construction and Building Materials*, vol. 228, p. 116 818, Dec. 2019. DOI: 10.1016/j.conbuildmat.2019.116818.

[19] Wikimedia Commons. "File:Seebeck effect circuit 2.svg — Wikimedia Commons, the free media repository." (2024), [Online]. Available: https://commons.wikimedia.org/w/index.php?title=File:Seebeck_effect_circuit_2.svg&oldid=934728259 (last visited on 07/23/2025).

[20] A. Z. Paydar, S. K. M. Balgehshiri, and B. Zohuri, "Heated junction thermocouple system," in *Advanced Reactor Concepts (ARC)*. Elsevier, 2023, pp. 341–380. DOI: 10.1016/b978-0-443-18989-0.00007-7.

[21] T. Guclu and E. Cuce, "Thermoelectric Coolers (TECs): From Theory to Practice," *Journal of Electronic Materials*, vol. 48, no. 1, pp. 211–230, Oct. 2018. DOI: 10.1007/s11664-018-6753-0.

[22] D. Krajewski, "Controller Design by Chien, Hrones and Reswick," 2021. [Online]. Available: https://www.researchgate.net/publication/354383003_Controller_Design_by_Chien_Hrones_and_Reswick/citation/download (last visited on 07/17/2025).

[23] Tark Thermal Solutions. "AA-150-24-44-LTS Datasheet," Tark Thermal Solutions. (Jun. 1, 2022), [Online]. Available: https://tark-solutions.com/products/thermoelectric-cooler-assemblies/peltier-air-conditioners/AA-150-24-44/pdf/ (last visited on 08/13/2025).

[24] Tark Thermal Solutions. "TC-XX-PR-59 Temperature Controller." (2025), [Online]. Available: https://tark-solutions.com/de/products/product-temperature-controllers/tc-xx-pr-59-temperature-controller (last visited on 08/13/2025).

[25] K. J. Åström and T. Hägglund, *PID controllers, theory, design, and tuning*, 2. ed. Research Triangle Park, NC: Instrument Society of America, 1995, 343 pp., Includes bibliographical references and index.

[26] E. Hasenjäger, *Regelungstechnik für Dummies* (Lernen einfach gemacht), 2. Auflage, F. Thuselt, Ed. Weinheim: Wiley-VCH Verlag GmbH Co. KGaA, 2019, 440 pp., Literaturangaben.

[27] MARUM Center for Marine Environmental Sciences. "Bremen Core Collection (Scientific Ocean Drilling Programs)." (n.d.), [Online]. Available: https://www.marum.de/en/Bremen-Core-Collection-Scientific-Ocean-Drilling-Programs.html (last visited on 08/18/2025).

A. Documentation of the Use of AI-based Tools and Applications

Table A.1: Use of AI-based tools and applications

AI-based Tool	**Purpose**	**Aspect of the Work Affected**	**Prompt**	**Comment**
ChatGPT	Check for grammar, orthography, and logical inconsistencies	Text passages	Check the following text passages for flaws in grammar, orthography and logical consistency. Don't generate full text passages. Instead create a list of aspects to improve.	The answer helped me polish already written text passages. Reviews and improvements were made manually.
ChatGPT	LaTeX table formatting	Tables	Create the LaTeX framework of a table with x rows and y columns.	The answer created well-formatted tables, that could be filled with data.
ChatGPT	Finding color codes	Figure 2.7	Give me a list of color codes used in the sample image.	The answer helped me create a figure in the same style as figures from a resource.

B. Technical Drawing of the Aluminum Frame

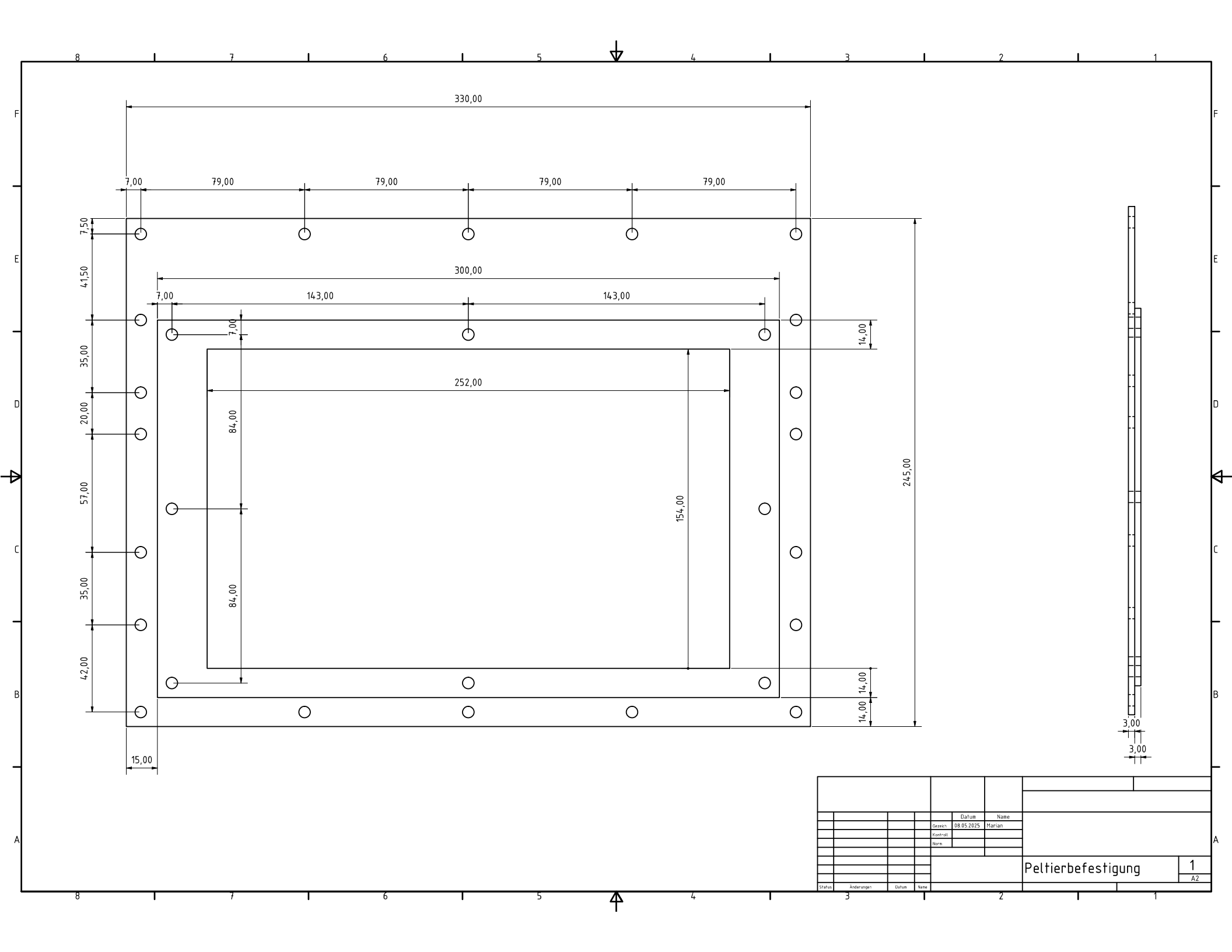
330,00
7,00
79,00
79,00
79,00
79,00
7,50
41,50
35,00
20,00
57,00
35,00
42,00
300,00
7,00
143,00
143,00
7,00
252,00
84,00
84,00
154,00
14,00
14,00
14,00
245,00
15,00
3,00
3,00
Datum
Name
Gezeich.
08.05.2025
Marian
Kontroll
Norm
Peltierbefestigung
1
A2
Status
Änderungen
Datum
Name